EDGE PLASMA PROPERTIES OF OHMIC DISCHARGES WITH RESONANT MAGNETIC PERTURBATIONS IN THE STOR-M TOKAMAK

A Thesis Submitted to the

College of Graduate Studies and Research

in Partial Fulfillment of the Requirements

for the Degree of Master of Science

in the Department of Physics and Engineering Physics

University of Saskatchewan

Saskatoon

By

Michael Hubeny

PERMISSION TO USE

In presenting this thesis in partial fulfilment of the requirements for a Postgraduate degree from the University of Saskatchewan, I agree that the Libraries of this University may make it freely available for inspection. I further agree that permission for copying of this thesis in any manner, in whole or in part, for scholarly purposes may be granted by the professor or professors who supervised my thesis work or, in their absence, by the Head of the Department or the Dean of the College in which my thesis work was done. It is understood that any copying or publication or use of this thesis or parts thereof for financial gain shall not be allowed without my written permission. It is also understood that due recognition shall be given to me and to the University of Saskatchewan in any scholarly use which may be made of any material in my thesis.

Requests for permission to copy or to make other use of material in this thesis in whole or part should be addressed to:

Head of the Physics and Engineering Physics Dept
University of Saskatchewan
116 Science Place
Saskatoon, SK S7N 5E2
Phone: (306) 966-6393
Fax: (306) 966-6400

ABSTRACT

Understanding and controlling cross-field transport caused by turbulence is a major challenge towards achieving the plasma confinement necessary to operate a thermonuclear fusion reactor. Measuring fluctuations of plasma density and potential in the edge of a toroidally confined plasma is important to characterize the turbulent transport and suppression mechanisms for turbulence.

A 16 pin rake probe is installed on the Saskatchewan Torus-Modified tokamak to measure density and potential with high temporal resolution. The array consists of 8 by 2 single Langmuir probes, which allow good radially and limited poloidally resolved measurements. Profiles of various plasma parameters were constructed for the edge and scrape off layer (SOL) to investigate different discharge scenarios.

The Resonant Magnetic Perturbations altered the plasma transport in the edge and SOL region, leading to a higher density pedestal and a potential drop in some cases. During an enhanced confinement phase, it was possible to identify a region where intermittent transport events are created and leave behind holes of lower density. The existence of the high-frequency branch of zonal flows, the geodesic acoustic mode, could not be verified conclusively. Increased coherence and amplitude of floating potential fluctuations in the frequency range of $f \approx 20$ kHz were found, but coherent Magnetohydrodynamic (MHD) oscillations indicated a substantial connection to the floating potential fluctuations in this frequency band, while MHD oscillations at higher frequency showed no connection.

ACKNOWLEDGEMENTS

I would like to thank my supervisor Prof. Chijin Xiao for his guidance and excellent support during my research. My co-supervisor Prof. Akira Hirose deserves great appreciation for his effort as a director of the Plasma Physics Laboratory. They both enabled me to enjoy a demanding research in a foreign country and it was a fantastic opportunity to study under their supervision.

Thanks to Dave McColl for keeping the lab sound and to the technical assistance by him and the physics machine shop, Perry Balon, Blair Chomyshen and Ted Toporowski. My fellow graduate students Sayf Gamudi Elgriw, Yue Ding and Postdoc Takumi Onchi and Mykola Dreval helped whenever needed and remain in friendship.

I would also like to thank my family and all my new friends in Saskatoon and Canada for their support and encouragement.

This research was supported by the grants from the Natural Sciences and Engineering Research Council of Canada (NSERC), Canada Research Chair (CRC) Program and through financial aid from the University of Saskatchewan Graduate Research Scholarship.

CONTENTS

LIST OF TABLES

List of Figures

List of Abbreviations and Symbols

CT	Compact torus
EEDF	Electron energy distribution function
GAM	Geodesic acoustic mode
H-mode	High confinement mode
HIBP	Heavy ion beam probe
MHD	Magnetohydrodynamics
OH	Ohmic heating
PDF	Probability density function
RF	Radio frequency
RMP	Resonant magnetic perturbation
RMS	Root mean square
STOR-M	Saskatchewan Torus Modified
STOR-1M	Saskatchewan Torus 1 Modified
SOL	Scrape off layer
ZF	Zonal flow
M, m	Ion and electron mass
n	Density
v	Velocity
E	Electric field
B	Magnetic field
r, θ, ϕ	Radial, poloidal and toroidal coordinates
a, R	Minor and major radii
ε	Inverse aspect ratio a/R
p	Pressure
ρ	Mass density
J	Current density
η	Resistivity
γ	Ratio of specific heats
k_{B}	Boltzmann constant
ε_0	Vacuum permittivity
μ_0	Vacuum permeability
ϕ	Potential
C_{s}	Speed of sound
τ_{e}	Energy confinement time
Γ	Flux
I_{P}	Plasma current
V_{l}	Loop voltage
ω	Frequency
S, K	Skewness and Kurtosis
ΔH	Horizontal plasma position
Z	Atomic number

CHAPTER 1

INTRODUCTION

1.1 Fusion

The world population has been growing exponentially due to improvements in medicine and nutrition, while at the same time the energy consumption per person has been rising due to a higher living standard. Thus, even if the population reaches an expected maximum in the middle of the 21st century, the global energy consumption will continue to grow as shown in Figure 1.1 (a). Conventional energy sources are depleting or harder to extract and renewable energy from wind or sun is not reliable enough without large scale storage systems. Providing the energy for a growing living standard without increasing the environmental impact will be a big challenge of the 21st century. Figure 1.1 (b) shows a possible electricity production scheme where fusion takes over a sizeable part in the second half of the century. Controlled nuclear fusion will provide a clean and essentially endless source of energy. Unlike in stellar cores, where gravity leads to high pressure and long confinement times, man-made fusion reactors have to use different means to achieve a controlled fusion reaction.

Essential for the feasibility of a fusion reactor is the temperature needed to reach a high cross-section for the fusing particles and to overcome the coulomb repulsion between them. Figure 1.2 shows cross-sections for a number of different fusion reactions with the deuterium and tritium reaction clearly dominating as the best candidate, because of its high cross-section at a relatively low temperature. Under consideration of a Maxwellian energy distribution, the high energy tail is responsible for most fusion reactions. Therefore, the plasma temperature can be 10-20 keV instead of 70 keV, which corresponds to the centre-of-mass kinetic energy with the maximum cross-section.

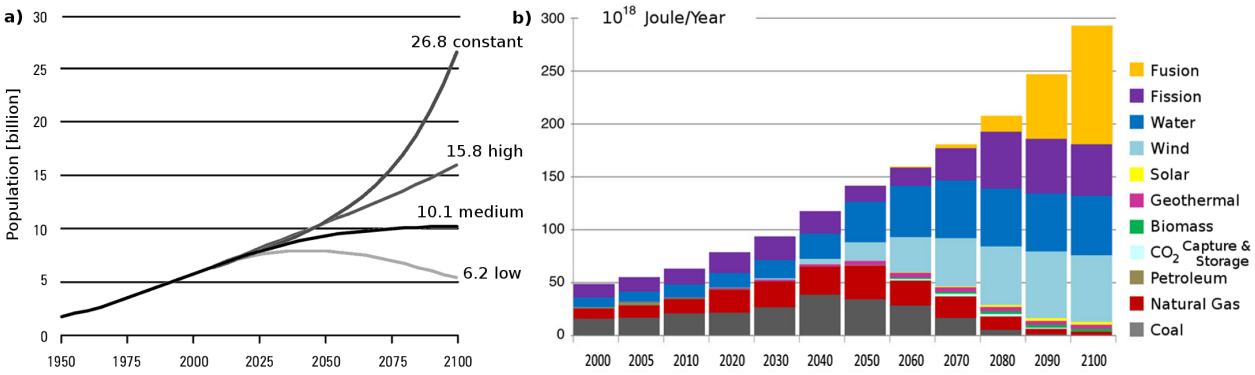

Figure 1.1: a) Global population estimates with different growth rates [1] and b) global electricity consumption based on a CO_2 limitation scenario of 550 ppm in the atmosphere [2].

The reaction between deuterium and tritium,

$$^2\mathrm{D} + {}^3\mathrm{T} \Rightarrow {}^4\mathrm{He} + \mathrm{n} + 17.6\ \mathrm{MeV}, \tag{1.1}$$

releases 17.6 MeV in total, where about a fifth of the energy, carried by the charged α particle, is potentially available to heat the plasma. The neutron escapes, since it has no charge and a low cross-section at high energies.

Deuterium is a stable isotope with a natural abundance of 0.016% of hydrogen, but tritium has a half-life of 12.3 years and is therefore not naturally occurring. A convenient method to produce tritium is using the neutrons from the fusion reaction to bombard lithium in the following way:

$$^6\mathrm{Li} + \mathrm{n} \Rightarrow {}^4\mathrm{He} + {}^3\mathrm{T} + 4.8\ \mathrm{MeV} \tag{1.2}$$

$$^7\mathrm{Li} + \mathrm{n} \Rightarrow {}^4\mathrm{He} + {}^3\mathrm{T} + n - 2.47\ \mathrm{MeV}. \tag{1.3}$$

Since the high neutron flux of the deuterium tritium fusion reaction damages and activates the materials of a fusion reactor, aneutronic fusion reactions are under research. The highest cross-section for reactions releasing no neutrons are the deuterium-helium and hydrogen-boron fuel cycles:

$$^2\mathrm{D} + {}^3\mathrm{He} \Rightarrow {}^4\mathrm{He} + \mathrm{p} + 18.3\ \mathrm{MeV} \tag{1.4}$$

$$\mathrm{p} + {}^{11}\mathrm{B} \Rightarrow 3\,{}^4\mathrm{He} + 8.7\ \mathrm{MeV}. \tag{1.5}$$

However, these reactions require a much higher plasma temperature to reach the maximum of the reaction cross-section, as can be seen in Figure 1.2. Therefore, aneutronic fusion reactions are only an option for reactors in the far future.

Although the path to develop a fusion reactor is planned long-term, there are critical issues that need to be controlled or solved before bigger reactors than the now existing ones are built. Since the beginning of experiments with magnetically confined plasmas, it has been observed that the rate at which particles diffuse across the magnetic field is higher than classical transport models predict, thus called anomalous transport. Complex countermeasures have been discovered (H-modes) [3] and developed (e.g. Resonant Magnetic Perturbations) to reduce particle and energy losses, to stabilize the plasma and to improve plasma parameters. Another key aspect is the first wall of a working fusion reactor. Scaling up the size of a fusion reactor leads to better volume to surface area ratio, but the higher plasma content can cause serious damage to the plasma facing walls. Current calculations predict heat/power loads of 1-10 MW/m^2 and peak power loads of up to 200 MW/m^2 at the wall and divertor [4]. Preventing erosion and degradation of the first wall is under active research, since it has direct influence on the lifetime of a fusion reactor.

Anomalous transport and the processes at the wall are connected by the new understanding of intermittent transport events, the so-called blobs. They are spots or bands along the magnetic field with increased density (and maybe temperature), which propagate from the deeper edge region towards the first wall. In this way they affect the transport at the plasma edge as well as the plasma wall interaction. It is not clear yet if the intermittent transport of blobs has a more detrimental effect than continuous transport, but sputtering of wall material or burying of tritium in the wall depends on the particle momentum (i.e. temperature).

1.2 Fusion Reactors

There are a number of different reactor designs developed over the last 30 to 40 years. On the one hand there are reactors that use inertial confinement in combination with lasers or particle beams to rapidly heat and compress pellets of fuel. They can reach high densities and temperatures, but the confinement time is the limiting factor, since the delay until the fuel is accelerated outwards is in the order of nano seconds [6]. Furthermore, the operation of those reactors is not continuous by design.

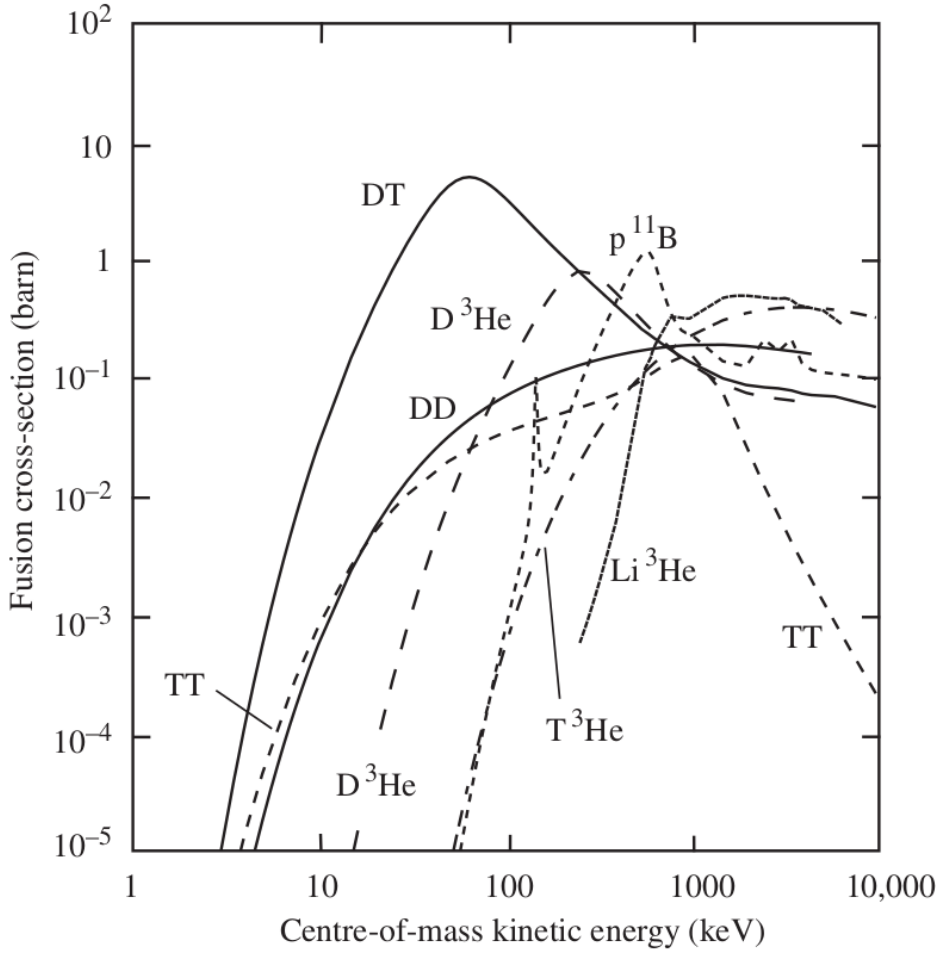

Figure 1.2: Cross-sections of different fusion reactions depending on particle energy [5].

On the other hand, a long history of research can be found for fusion reactors with magnetically confined plasmas. From the various subgroups of reactors, that make use of this principle the most promising candidates are the stellarator and the tokamak. Stellarators have a complex shape and are therefore difficult to construct, but can operate continuously, without the need of current drive [7]. However, the tokamak concept has received the most attention in fusion research and is therefore the most advanced design. Also the majority of fusion test devices are tokamaks, thus the understanding of the physics in this confinement geometry is better.

A conceptual drawing in Figure 1.3 shows how a final reactor could operate. Deuterium and Tritium are heated up initially by the plasma current and other external sources. The current is needed during the operation in addition to the magnetic coils to create the magnetic confinement. The α-particles heats the plasma, while the neutrons are not confined and leave the burning chamber. They heat the blanket and react with the lithium inside to fulfil two basic needs: First, the heat that is absorbed in the blanket is used to power a generator that creates electricity and second, the neutrons create tritium according to equation 1.2. Tritium is radioactive, short lived and very expensive, so it is beneficial to produce it on site in such a closed system. Helium is the "ash" of the fusion process and needs to be removed from the chamber.

1.3 Tokamak

One of the many fusion reactor designs is the tokamak, where the plasma is magnetically confined in a torus shaped vacuum chamber. The name is from the russian language and means **to**roidal'naya **ka**mera s **ma**gnitnymi **k**atushkami – toroidal chamber in magnetic coils. The concept and first experiments were made in the early 50's by the soviet physicists Igor Tamm and Andrei Sakharov at the Kurchatov Institute [9].

The toroidal magnetic field, pointing along the major revolution, confines charged particles through the Lorentz force and is created by coils enclosing the vacuum chamber. Due to the geometry there is an intrinsic gradient of the magnetic field, since the distance between the coils is larger in the outer part of the chamber than in the inner part. Without countermeasures the plasma would experience a charge separation by the gradient drift, which in turn creates another drift called $E \times B$ drift. The charge separation creates an electric field along the vertical direction, causing an $E \times B$

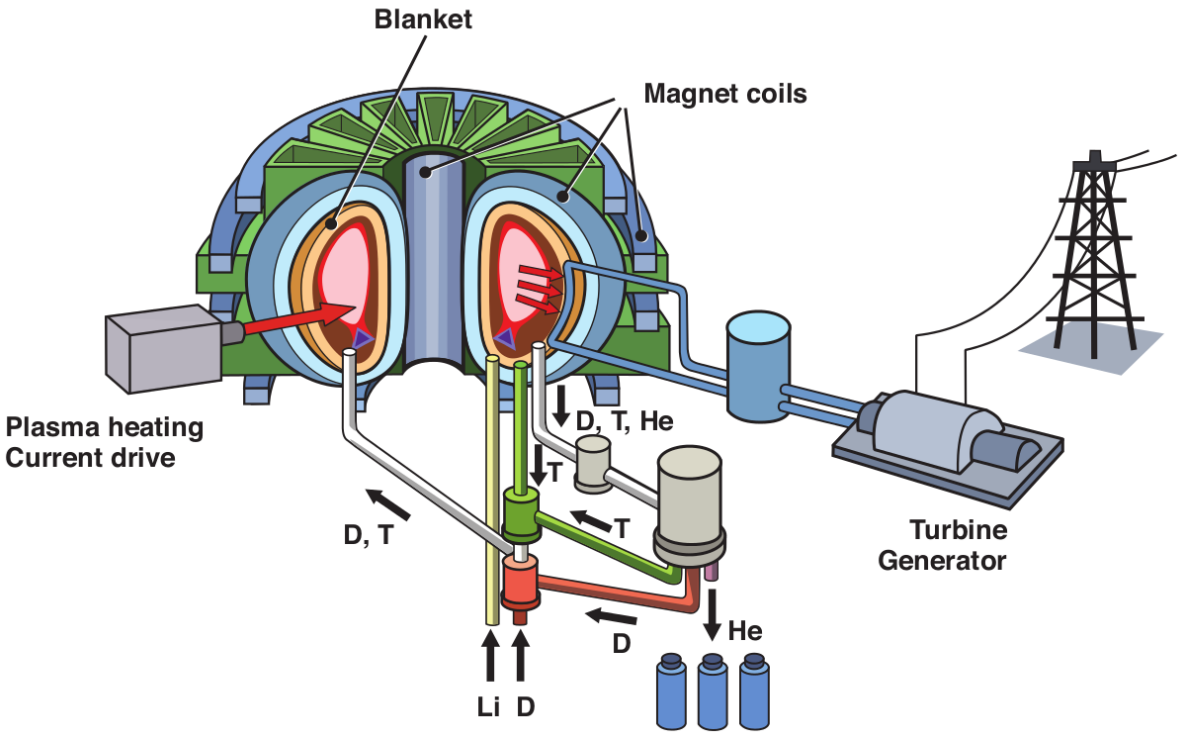

Figure 1.3: Schematic design of a fusion reactor with its main components [8].

drift towards the wall and a loss of confinement [10].

The solution is a poloidal magnetic field created by an induced toroidal current, using the plasma as the second winding of a transformer. There are also non-inductive ways to drive a current, but the former is an efficient heating method for plasma at lower temperatures. The magnetic field requirements result in the basic form of a tokamak shown in Figure 1.4, where the parts are denoted.

The plasma extent is either restricted by a limiter, which physically limits the plasma with a metal plate or a magnetic field configuration, that creates an X-point in the magnetic field leads the open field lines towards a metal plate called divertor. The region outwards of the last closed flux surface is called scrape of layer (SOL) and the separatrix is the region outside the last closed flux surface and X-point in a divertor configuration.

1.4 Motivation and Objectives

The main objectives and research motivation for this thesis are the following points:

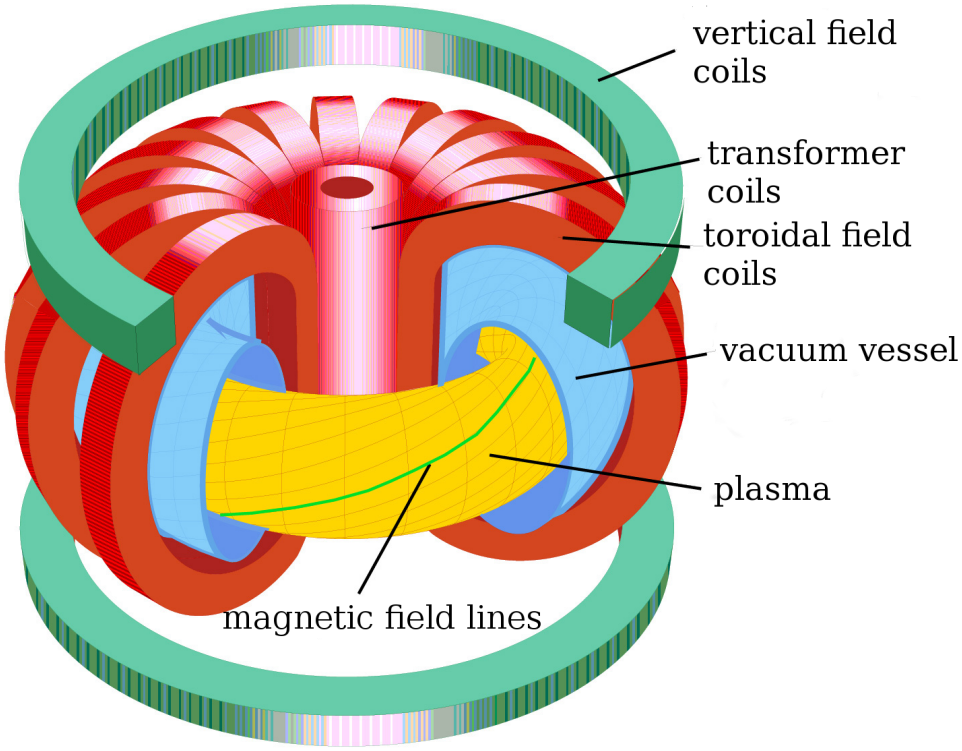

Figure 1.4: Tokamak device scheme, adapted from the 'German Physical Society' (DPG) [11].

- Build and install a rake probe on Saskatchewan Torus - Modified with all necessary electronic components, modifying and repairing if required.
- Measure and characterize spatial and spectral features of equilibrium edge parameters during normal Ohmic discharge on STOR-M.
- Investigate the existence and location of coherent fluctuation modes and intermittent transport events.
- Study the effect of Magnetohydrodynamic suppression on the edge parameters by employing Resonant Magnetic Perturbation coils.

1.5 Thesis Outline

The background of nuclear fusion and the current development of fusion reactors was described in this Chapter. The following Chapter deals with the theoretical background of plasma in a magneti-

cally confined system. Firstly, the MHD theory is introduced and then used to describe phenomena related to the results that are presented in this thesis, namely the geodesic acoustic mode and drift waves.

The first part of Chapter 3 describes the STOR-M tokamak and its major components and operational aspects. In the second part of Chapter 3, Sections 3.4 to 3.9, the main diagnostic equipment is presented briefly, while the Langmuir probe is explained in detail.

Chapter 4 contains the description of the data acquisition system and highlights the signal processing techniques.

The results of this research are presented in Chapter 5. In the first Section, typical ohmic discharges are analysed and profiles of the relevant properties are presented. Afterwards, evidence for the existence of the geodesic acoustic mode in STOR-M are shown and discussed. The influence of the RMP on edge parameters is evaluated in the subsequent Sections, first on density, floating potentials and derived properties.

Chapter 6 summarizes the major findings of this work and gives future work suggestions in terms of probes, data analysis and tokamak operation.

CHAPTER 2

THEORY

2.1 Magnetohydrodynamic Theory

One of the basic theoretical frameworks to describe plasma is Magnetohydrodynamic (MHD) theory. It combines the fluid-like description of a dense gas with the collective motion of charged particles. The response to magnetic and electric fields, which are imposed on the plasma, can be solved macroscopically for a bulk plasma with sufficient particles and density to justify a fluid treatment. Plasma can be described as either one fluid or as two fluids, electrons and ions, permeating each other. The equilibrium density of both species is assumed to be equal for the spatio-temporal limits set by collisions and particle inertia. Beyond those limits plasma waves can induce small differences in plasma density. In general, collisions between particles create a nearly Maxwellian velocity distribution of the particles. In ideal MHD theory all dissipative effects like viscosity or resistivity are ignored.

In the following, a basic set of equations to describe a two fluid plasma is given. The equation of motion for ions and electrons reads

$$M\,n\left(\frac{\partial}{\partial t}+\vec{v}_\mathrm{i}\cdot\nabla\right)\vec{v}_\mathrm{i} = \quad n\,e\,\vec{E}+e\,n\,\vec{v}_\mathrm{i}\times\vec{B}-\nabla p_\mathrm{i} \tag{2.1}$$

$$m\,n\left(\frac{\partial}{\partial t}+\vec{v}_\mathrm{e}\cdot\nabla\right)\vec{v}_\mathrm{e} = -n\,e\,\vec{E}-e\,n\,\vec{v}_\mathrm{e}\times\vec{B}-\nabla p_\mathrm{e}, \tag{2.2}$$

where M is the ion and m the electron mass, v_i is the ion and v_e the electron velocity, n is the plasma density, e is the electron charge, $\vec{E}$ is the electric field and p_i and p_e are the ion and electron pressures, respectively. Here, the ion and electron pressure are assumed to be isotropic, while in a more detailed description the pressure along and across the magnetic field can differ due to different temperatures.

Since the mass of the electron can be neglected compared to M, the mass density can be approximated by $\rho = (M+m)n \approx Mn$. Similar to the mass density, the ions are responsible for most of the mass flow due to their higher mass, thus the average speed $\vec{v}$ of the total mass flow can be simplified to:

$$\vec{v} = \frac{M\vec{v}_\mathrm{i} + m\vec{v}_\mathrm{e}}{M+m} \approx \vec{v}_\mathrm{i}. \tag{2.3}$$

Equations 2.1 and 2.2 are added to obtain

$$\rho\left(\frac{\partial}{\partial t} + \vec{v}\cdot\nabla\right)\vec{v} = \vec{J}\times\vec{B} - \nabla p, \tag{2.4}$$

where $\vec{J}$ is the current density

$$\vec{J} = n\ e(\vec{v}_\mathrm{i} - \vec{v}_\mathrm{e}) \tag{2.5}$$

and the total pressure p is the sum of the ion and electron partial pressures

$$p = p_\mathrm{i} + p_\mathrm{e}. \tag{2.6}$$

Ohm's law in resistive MHD is

$$\vec{E} + \vec{v}\times\vec{B} = \eta\vec{J}, \tag{2.7}$$

while in ideal MHD the resistivity η is zero.

The individual particle continuity equations for ions and electrons,

$$\frac{\partial n_\mathrm{i,e}}{\partial t} + \nabla\cdot(n_\mathrm{i,e}\vec{v}_\mathrm{i,e}) = 0, \tag{2.8}$$

can be used to derive the total mass continuity equation, if ion and electron mass are multiplied with equation 2.8 for ions and electrons, respectively. Adding the equations yields

$$\frac{\partial \rho}{\partial t} + \nabla\cdot(\rho\vec{v}) = 0. \tag{2.9}$$

Furthermore, the equation of state connects pressure to the density:

$$p = C\rho^\gamma, \tag{2.10}$$

where $\gamma = C_p/C_V$ is the ratio of the specific heats and C is a constant. In the presence of a magnetic field the value of γ can depend on the direction in respect to the magnetic field and ranges between unity for an isothermal compression and larger values depending on the degrees of freedom N

$$\gamma = \frac{2+N}{N}. \tag{2.11}$$

A monatomic gas has three translational degrees of freedom and thus $\gamma = 5/3$, while diatomic gases have additional rotational degrees of freedom with $\gamma = 7/5$. A strong magnetic field can reduce the degrees of freedom to $N = 2$ by forcing charged particles on a rotating trajectory, if the collisionality of the plasma species is not scattering the gyrating trajectories.

As the ideal MHD equations describe a single fluid, only equations 2.4, 2.9 and 2.10 are part of this description. To close this system of equations, Maxwell's equations have to be included with approximations for plasma, i.e. the displacement current and the net charge are negligible:

$$\nabla \times \vec{B} = \mu_0 \vec{J} \tag{2.12}$$

$$\nabla \times \vec{E} = -\frac{\partial \vec{B}}{\partial t} \tag{2.13}$$

$$\nabla \cdot \vec{B} = 0 \tag{2.14}$$

$$\nabla \cdot \vec{E} = 0. \tag{2.15}$$

In order to derive the basic fluid drifts, the generalized form of equations 2.1 and 2.2 with subscript j denoting the species is considered in equilibrium ($\partial/\partial t = 0$). Small velocities in respect to the sound speed C_s are assumed, so the second order $(\vec{v}_j \cdot \nabla \vec{v}_j)$ term can be neglected. Finally, taking the cross product with $\vec{B}$ yields the components perpendicular to the magnetic field:

$$\begin{aligned} 0 &= q_j \, n_0 \, (\vec{E} \times \vec{B} + (\vec{v}_j \times \vec{B}) \times \vec{B}) - \nabla p_j \times \vec{B} \\ 0 &= q_j \, n_0 \, (\vec{E} \times \vec{B} - \vec{v}_{j,\perp} B^2) - \nabla p_j \times \vec{B}, \end{aligned} \tag{2.16}$$

where $\vec{v}_{j,\perp}$ is the velocity component perpendicular to the magnetic field. Solving for $\vec{v}_{j,\perp}$

$$\vec{v}_{j,\perp} = \frac{\vec{E} \times \vec{B}}{B^2} - \frac{\nabla p_j \times \vec{B}}{q_j \, n_0 B^2} = \vec{v}_{E \times B} + \vec{v}_{j,\mathrm{Dia}}, \tag{2.17}$$

where n_0 is the equilibrium plasma density and $\vec{v}_{j,\mathrm{Dia}}$ is the diamagnetic drift velocity, sometimes denoted as v_j^*. While the $E \times B$ drift $\vec{v}_{E \times B}$ is independent of charge q and therefore does not cause any current, the diamagnetic drift can create a current since the sign for electrons and ions is opposite. Another basic difference is that no particle moves with the diamagnetic drift velocity, because $\vec{v}_{\mathrm{Dia}}$ is fluid drift, but not a particle or guiding centre drift. In a pictorial description the diamagnetic drift is caused by a different number of gyrating particles along a density gradient, as shown in Figure 2.1. The area within the rectangle contains a net current pointing upwards, without

a particle actually moving in this direction. Without a temperature gradient the diamagnetic drift can be simplified to

$$\vec{v}_{j,\mathrm{Dia}} = -\frac{k_\mathrm{B} T_j}{q_j \, n_0 \, B^2} \nabla n_0 \times \vec{B} \tag{2.18}$$

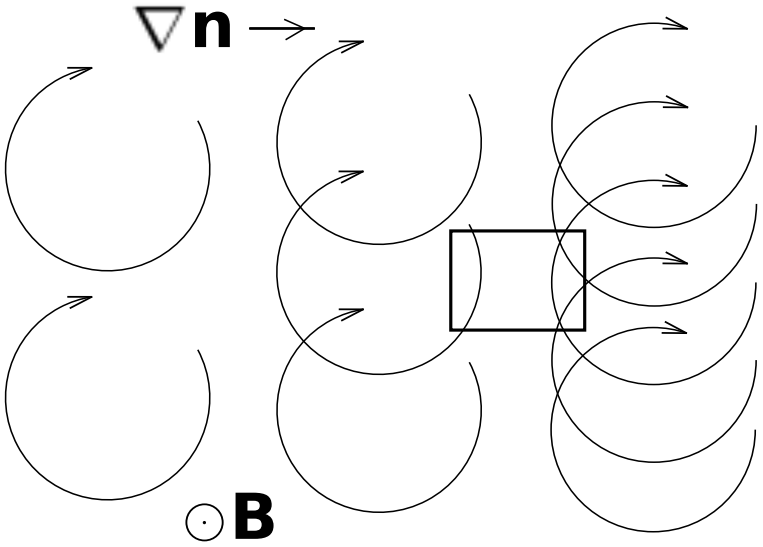

Figure 2.1: Gyrating particles with a density gradient, creating the diamagnetic drift.

Radial Force Balance

Considering the equation of motion for ions 2.1 in equilibrium, i.e. $\partial/\partial t = 0$ and neglecting the convective term $(\vec{v} \cdot \nabla \vec{v})$, it can be simplified to

$$n_0 \, e \, \vec{E} + n_0 \, e \, \vec{v} \times \vec{B} - \nabla p_\mathrm{i} = 0. \tag{2.19}$$

Explicitly writing the radial components leads to the radial electric field

$$E_r = \frac{1}{n_0 \, e} \frac{\partial p_\mathrm{i}}{\partial r} - (\vec{v} \times \vec{B}) \cdot \vec{e}_r = \frac{1}{n_0 \, e} \frac{\partial p_\mathrm{i}}{\partial r} - v_\phi B_\theta + v_\theta B_\phi, \tag{2.20}$$

where θ and ϕ denote the poloidal and toroidal direction of the torus as shown in Figure 2.2. This equation connects a radial electric field with the pressure gradient and poloidal and toroidal flow. In the edge regions all of the quantities in equation 2.20 can be measured by different internal probes. The electric field and the flows play an important role in suppressing convecting structures or intermittent events by sheared flows related to a sheared $E \times B$ drift. A steeper pressure gradient in equilibrium leads to and is also a result of a better energy confinement in the plasma.

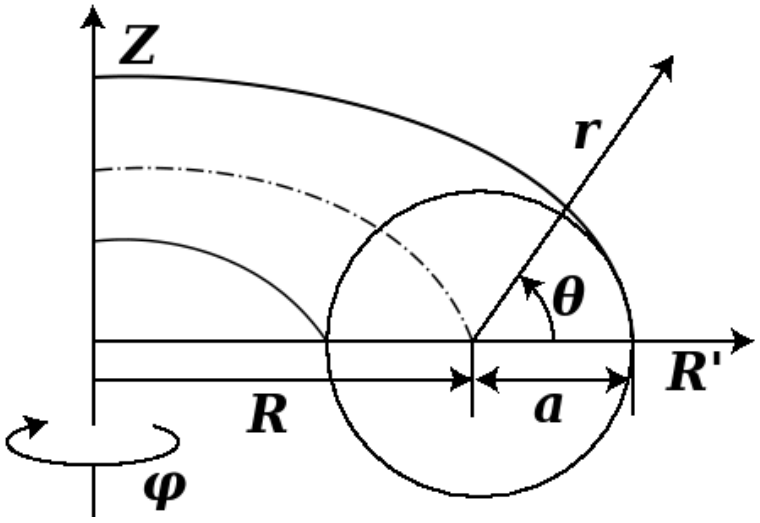

Figure 2.2: Toroidal coordinate system consists of the minor radius r, poloidal angle θ and the toroidal angle ϕ directed clockwise or pointing out of the page. R denotes the major radius of the tokamak and R' and Z the major radius and vertical direction, respectively.

Electron Dynamics Parallel to the Magnetic Field

The z direction of equation 2.2 shows the electron dynamics along the magnetic field:

$$m\,n\left(\frac{\partial v_z}{\partial t}+(v\cdot\nabla)v_z\right)=q\,n\,E_z-\frac{\partial p}{\partial z}. \tag{2.21}$$

The inertia terms on the left side are negligible, since the electron mass is small. Furthermore, the electron temperature along the magnetic field is not perturbed, leading to:

$$0=qnE_z-\gamma\,k_\mathrm{B}T_\mathrm{e}\frac{\partial n}{\partial z} \tag{2.22}$$

$$e\frac{\partial\phi}{\partial z}=\frac{\gamma\,k_\mathrm{B}T_\mathrm{e}}{n}\frac{\partial n}{\partial z}, \tag{2.23}$$

where $\vec{E}=-\nabla\phi$ and $q=-e$ has been substituted.

Due to their small inertia an isothermal response can be assumed for electrons and thus $\gamma=1$. Integration on both sides yields:

$$\frac{n_\mathrm{e}}{n_0}=\exp\left(\frac{e\phi}{k_\mathrm{B}T_\mathrm{e}}\right), \tag{2.24}$$

which is the Boltzmann relation. Therefore, changes in density lead to an immediate response in electrostatic potential and pressure in the toroidal direction.

2.2 Transport/Turbulence

In tokamaks the transport of particles and energy is closely linked to particle and energy confinement. Essential is the transport across the magnetic field lines, since charged particles are almost freely moving along the magnetic field lines. First expectations were based on collisions and the diffusion they cause. Charged particles gyrate with the Larmor radius around a line of force and collisions can change their centre of gyrating trajectory, resulting in cross-field transport. This is similar to a random walk process with the Larmor radius as a step length, so it can be described as a classical diffusive process.

The most probable cause of anomalous transport in confined plasmas is drift wave turbulence. Since the instability that leads to drift waves is caused by a pressure gradient, it is present in most plasma devices and also called universal instability. They are predominantly propagating along the poloidal direction in a tokamak and form a broad spectrum of turbulence visible in the local plasma density and potential fluctuations [12].

A pictorial explanation and a brief derivation in a slab/cartesian geometry follows. A small poloidal cut is approximated in a slab/cartesian geometry to show the basic concept of a drift wave. The magnetic field is pointing in the z or toroidal direction, while the density gradient is towards the negative x-direction. Perturbed quantities $\tilde{f}$ are assumed to have a wavelike character: $\tilde{f} \sim e^{-i(\omega t - \vec{k}\cdot\vec{r})}$. The temperature is assumed to be constant and with a zero equilibrium electric field, the drift velocities are

$$\vec{v}_{\mathrm{i},0} = \vec{v}_{\mathrm{Dia,i}} = \quad \frac{k_\mathrm{B} T_\mathrm{i}}{n_0\, e\, B_0} \frac{\partial n_0}{\partial x} \vec{e}_y \tag{2.25}$$

$$\vec{v}_{\mathrm{e},0} = \vec{v}_{\mathrm{Dia,e}} = -\frac{k_\mathrm{B} T_\mathrm{e}}{n_0\, e\, B_0} \frac{\partial n_0}{\partial x} \vec{e}_y. \tag{2.26}$$

The electron dynamics along the magnetic field are determined by the Boltzmann relation, which can be linearised and rearranged as:

$$\frac{\tilde{n}_\mathrm{e}}{n_0} = \frac{e\tilde{\phi}}{k_\mathrm{B} T_\mathrm{e}}, \tag{2.27}$$

where $\tilde{n}$ and $\tilde{\phi}$ are the fluctuating parts of the density and potential. The perturbed $E \times B$ velocity in this geometry is given by:

$$\tilde{v}_x = \frac{E_y}{B_0} = \frac{-ik_y\, \tilde{\phi}}{B_0}. \tag{2.28}$$

Considering only the guiding centres, the equation of continuity is:

$$\frac{\partial \tilde{n}}{\partial t} = -\tilde{v}_x \frac{\partial n_0}{\partial x}. \tag{2.29}$$

Higher order terms for the convective part have been omitted. Combining the last three equations gives:

$$-i\,\omega\,\tilde{n} = \frac{ik_y\,\tilde{\phi}}{B_0}\frac{\partial n_0}{\partial x} = \frac{-i\omega\,e\,\tilde{\phi}}{k_\mathrm{B}T_\mathrm{e}} n_0, \tag{2.30}$$

Rearranging yields the phase velocity:

$$\frac{\omega}{k_y} = -\frac{k_\mathrm{B}T_\mathrm{e}}{n_0\,e\,B_0}\frac{\partial n_0}{\partial x} = v_\mathrm{Dia,e}. \tag{2.31}$$

Therefore, the wave travels with the electron diamagnetic drift velocity, where the name drift wave stems from.

Considering resistivity, the potential will not be 90° shifted anymore, thus ω will be complex. An approximate dispersion relation [10] reads

$$\omega \approx \omega_\mathrm{Dia} + \frac{i\omega_\mathrm{Dia}^2}{\sigma_\parallel}, \tag{2.32}$$

where $\sigma_\parallel$ is a normalized collision frequency. The sign of the imaginary part is always positive, i.e. the wave will grow, whenever there is a density gradient and finite resistivity in the plasma.

In Figure 2.3, the structure of the drift waves is shown. On the left side a cylindrical cut is shown, where the phase follows the helical magnetic field lines. The region in the rectangle is shown on the left side in cartesian coordinates. The homogeneous magnetic field points out of the plane and is perpendicular to the density gradient, indicating a higher density in the lighter grey shaded area. A small density variation would initially not lead to charge creation, but due to their small masses electrons move quickly along the magnetic field lines. This is caused by the relation between increased potential and density described by the Boltzmann relation. Since the ions remain at their position, they create a charge of ions and electrons in different locations. An electric field $\tilde{E}_y$ forms between the two charges, which in turn creates a local $E \times B$ drift around the density perturbation. The perturbations modify the equilibrium density locally and the solid black boundary in Figures 2.3 b) and c) shows the resulting isodensity line. As noted in Figure 2.3 b) the $E \times B$ drift pushes plasma in the $\pm$x direction and due to the density gradient the perturbation will propagate in the y direction. In the linearly stable picture the Boltzmann equation is valid and thus

the density and potential are in phase. If due to collisions or other effects the potential is delayed, the $E \times B$ drift will amplify the perturbation and thus lead to instability as shown in Figure 2.3 c).

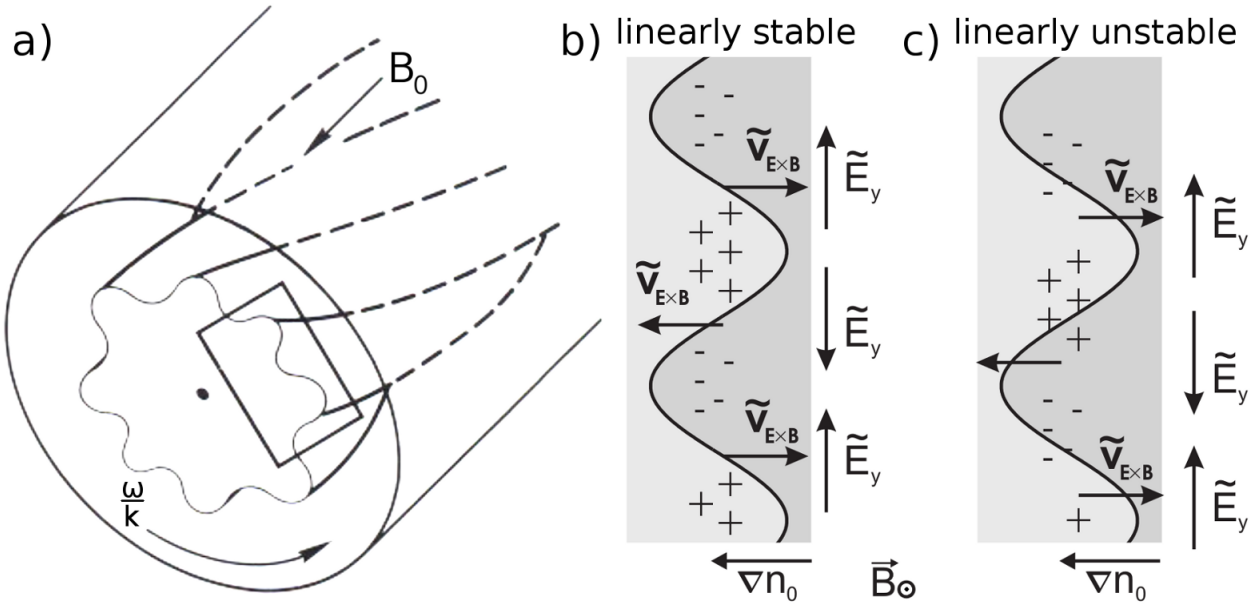

Figure 2.3: Illustration of drift wave fluctuations in a cylinder (a) and in slab geometry (b and c) [10, 13].

2.3 Zonal Flows and Geodesic Acoustic Mode

The geodesic acoustic mode (GAM) is a branch of zonal flows with a distinct low-frequency oscillation. The first analytical investigation of the GAM was done by *Winsor et al.* in 1968 [14]. The basic model uses MHD in the limit of a compressible fluid in the low pressure regime. The main equations are the continuity equation and the equation of motion:

$$\frac{\partial \tilde{\rho}}{\partial t} + \rho_0 \nabla \cdot \tilde{v} = 0 \tag{2.33}$$

$$\rho_0 \frac{\partial \tilde{v}}{\partial t} = \tilde{J} \times \vec{B} - \nabla \tilde{p}, \tag{2.34}$$

where $\tilde{v}$, $\tilde{j}$ and $\tilde{p}$ are the perturbed flow velocity, current and pressure, $\tilde{\rho}$ and ρ_0 are the perturbed and equilibrium mass density, respectively. The crucial feature is the compressibility of plasma, which is also important for deriving the sound velocity in a plasma. The toroidal magnetic field has a gradient in the radial direction due to the toroidal arrangement of the coils and is described by $B_\phi = B_0/(1 + \frac{a}{R}\cos\theta)$, where a and R are the minor and major radius, respectively. B_0 is the

toroidal magnetic field at the centre line axis. In the edge region of a confined plasma the $E \times B$ drift creates a poloidal flow, which depends on the magnetic field:

$$\tilde{v} = \frac{\tilde{E} \times \vec{B}}{B^2} \tag{2.35}$$

$$\begin{aligned} \nabla \cdot \tilde{v} &= -2\frac{\tilde{E} \times \vec{B}}{B^3} \cdot \nabla B \\ &= -2\frac{\tilde{E} \times \vec{B}}{B^3} \cdot \left(-\frac{B_0}{R}(\cos\theta \vec{e_r} - \sin\theta \vec{e_\theta}) \right) \\ &\simeq \quad 2\frac{\tilde{E} \times \vec{B}}{B^2 R} \cdot (\cos\theta \vec{e_r} - \sin\theta \vec{e_\theta}), \end{aligned} \tag{2.36}$$

where $\tilde{E}$ is the perturbed electrical field. The dominant components of electric and magnetic field are assumed to be in the radial and toroidal direction, respectively, thus leading to a poloidal drift. With the final result for $\nabla \cdot \tilde{v}$ plugged into equation 2.33, it becomes:

$$\begin{aligned} &\frac{\partial \tilde{\rho}}{\partial t} - 2\rho_0 \frac{(\tilde{E} \times \vec{B}) \cdot \vec{e_\theta}}{B^2 R} \sin\theta = 0 \\ &\frac{\partial \tilde{\rho}}{\partial t} + 2\rho_0 \frac{(\nabla_\perp \tilde{\phi} \times \vec{B}) \cdot \vec{e_\theta}}{B^2 R} \sin\theta = 0 \\ &\frac{\partial \tilde{\rho}}{\partial t} = 2\rho_0 \frac{i\, k_r\, \tilde{\phi}}{B} \frac{\sin\theta}{R} \end{aligned} \tag{2.37}$$

where $\tilde{\rho} = M\tilde{n}$ is proportional to $\sin\theta$. That leads to no detectable density fluctuations on the low and high field side ($\theta = 0, \pi$) and to a maximum amplitude on the top and bottom of the torus. This sinusoidal dependency is also called the $m = 1$ poloidal mode number.

In the derivation by *Winsor et al.* the charge neutrality is given as

$$\nabla \cdot \tilde{J_\perp} = 0, \tag{2.38}$$

where $\tilde{J_\perp}$ is the cross-field current, while the parallel current $\tilde{J_\parallel}$ is ignored. Multiplying equation 2.34 with $\vec{B}\times$ from the left side yields the cross-field components of all terms:

$$\tilde{J_\perp} = \frac{\rho_0}{B^2} \frac{\partial \tilde{E_\perp}}{\partial t} + \frac{\vec{B} \times \nabla \tilde{p}}{B^2}. \tag{2.39}$$

This can be plugged into the charge neutrality equation 2.38 to give

$$\begin{aligned}
\frac{\rho_0}{B^2}\frac{\partial \nabla \tilde{E}_\perp}{\partial t} + \nabla \cdot \left(\frac{\vec{B} \times \nabla \tilde{p}}{B^2} \right) &= 0 \\
\frac{\rho_0}{B^2}\frac{\partial(-\nabla_\perp^2 \tilde{\phi})}{\partial t} &= 2\frac{\nabla B}{B^3}\left(\vec{B} \times \nabla \tilde{p}\right) \\
\frac{\rho_0 k_r^2}{B^2}\frac{\partial \tilde{\phi}}{\partial t} &= 2\frac{\sin\theta}{B^2 R}\left(\vec{B} \times \nabla \tilde{p}\right)_\theta \\
\frac{\rho_0 k_r^2}{B^2}\frac{\partial^2 \tilde{\phi}}{\partial t^2} &= 2\frac{\sin\theta}{B^2 R}\left(\vec{B} \times \nabla \frac{\partial \tilde{p}}{\partial t}\right)_\theta,
\end{aligned} \tag{2.40}$$

where the same derivative of the magnetic field as in equation 2.36 has been used. The pressure perturbation can be related to the mass density as follows:

$$\tilde{p} = \gamma \frac{p_0}{\rho_0}\tilde{\rho}. \tag{2.41}$$

Using equations 2.41 and 2.37 in equation 2.40 with the substitution of all time and space derivatives leads to

$$\frac{\rho_0 k_r^2}{B^2}\omega^2 \tilde{\phi} = 2\frac{\sin\theta}{B^2 R}\left(B\, \gamma \frac{p_0}{\rho_0} 2\rho_0 \frac{k_r^2}{B}\tilde{\phi}\frac{\sin\theta}{R}\right) \tag{2.42}$$

$$\omega^2 = \frac{4\sin^2\theta}{R^2}\frac{\gamma p_0}{\rho_0}, \tag{2.43}$$

where the average of $\sin^2\theta$ is 1/2. This results in the dispersion relation of GAM:

$$\omega_{\mathrm{GAM}}^2 = \frac{2c_s^2}{R^2}, \tag{2.44}$$

where $c_s = \sqrt{\gamma p_0/\rho_0}$ is the speed of sound. The dispersion relation of the conventional sound wave

$$\omega = \frac{c_s}{qR} \tag{2.45}$$

modifies GAM and yields

$$\omega_{\mathrm{GAM}}^2 = \left(2 + \frac{1}{q^2}\right)\frac{c_s^2}{R^2} \tag{2.46}$$

for the whole dispersion relation.

The GAM oscillation has been observed in a number of tokamaks in the range of $f_{\mathrm{GAM}} = 15$-30 kHz in floating potential and plasma density [15, 16, 17]. It is located in the edge region of tokamaks very close to the limiter or the separatrix in divertor configurations. Larger and middle-sized tokamaks investigated zonal flows and GAMs extensively, while not all smaller tokamaks

found evidence for the existence of GAMs. Potential fluctuation measurements using a Heavy Ion Beam Probe (HIBP) detected signatures of GAM in the small tokamak TUMAN-3M [18]. Another tokamak, similar to STOR-M in size and operation parameters, found long ranged correlations of coherent structures in the edge region [19], but could not find the characteristic oscillation in the fluctuation spectra.

The increasing interest in ZFs and GAM was caused by the influence on turbulent transport and the level of turbulence in the plasma edge, where transport barriers are formed [20]. While investigating the generation of GAMs in different theoretical models [21, 22], the original derivation in the ideal MHD picture appeared to be flawed due to omitting the parallel current $\vec{J}_{\|}$. However, since GAMs have been found in the edge of tokamaks, the parallel current must be subject to a reduction possibly caused by the high collisionality in this region. Therefore, the derivation by *Winsor et al.* describes only a simplified picture, while for understanding the generation and impact of GAM a proper analysis is needed.

A pictorial explanation of the GAM is that a flow beginning at the low field side will be compressed on the way to the high field side, experiencing the highest effect while flowing parallel to the magnetic gradient: at the top and bottom side of the tokamak. The compression of the flow causes a density accumulation, resulting in an oscillation between a current and an electric field counteracting the accumulation. In the case of a stationary zonal flow there is a flow in the toroidal direction to compensate for the compression. In Table 2.1 some characteristics of the stationary zonal flows and geodesic acoustic mode are compared.

	Stationary Zonal Flow	GAM
Density fluctuations	0	$\frac{\tilde{n}}{n} = \left(\sqrt{2}k_r\rho_s\frac{e\tilde{\Phi}}{T_e}\right)\sin\theta$
Frequency	0	$\frac{c_s}{R}\sqrt{2+\frac{1}{q^2}}$
Radial wavelength	$\sqrt{r\rho_s}$	$\sqrt{r\rho_s}$
Mode numbers	$m = n = 0$	$m = 1(\tilde{n}), m = 0(\tilde{\Phi})$ $n = 0$

Table 2.1: Characteristic quantities of stationary ZF and GAM [16], where ρ_s is the Larmor radius at electron temperature and k_r is the radial wavenumber.

CHAPTER 3

EXPERIMENTAL SETUP

3.1 STOR-M

The Saskatchewan Torus-modified (STOR-M)[23] is a small tokamak for plasma fusion research at the University of Saskatchewan. It was built in 1987 as the replacement of the STOR-1M tokamak and is currently the only fusion research device in Canada. An upgrade in 1994 increased the strength of the toroidal field system. With over 250,000 shots STOR-M contributed to fusion research in various experimental settings like H-mode transition by turbulent heating [24], plasma biasing [25] or compact toroid (CT) injection [26]. The latter served more recently to investigate a novel method of fuelling a fusion reactor. Furthermore, MHD and density fluctuations as well as plasma flow measurements have been performed. The main parameters of the STOR-M tokamak are shown in Table 3.1. The positions of the currently used diagnostic systems are indicated in Figure 3.1, which shows the STOR-M tokamak in top view and a cross-section of the limiter. Other main components like the gas feed, pump and CT port are shown as well.

3.2 Vacuum Chamber and Gas Feed System

Two stainless steel (304L) pipe elbows with circular cross-section form the base of the vacuum chamber. The two halves are each connected by flexible bellows and a ceramic break to prevent mechanical stress and induction of current in the chamber. The vacuum chamber wall has a thickness of 4 mm and numerous ports welded on to provide access for diagnostics, gas feed system, pumping and the compact torus injector. The plasma radius is restricted by a stainless steel limiter consisting of a circular part with a radius of 13 cm and a horizontal rail at 12 cm. Thus a circular plasma with a minor radius of 12 cm can move ± 1 cm horizontally without being scraped off.

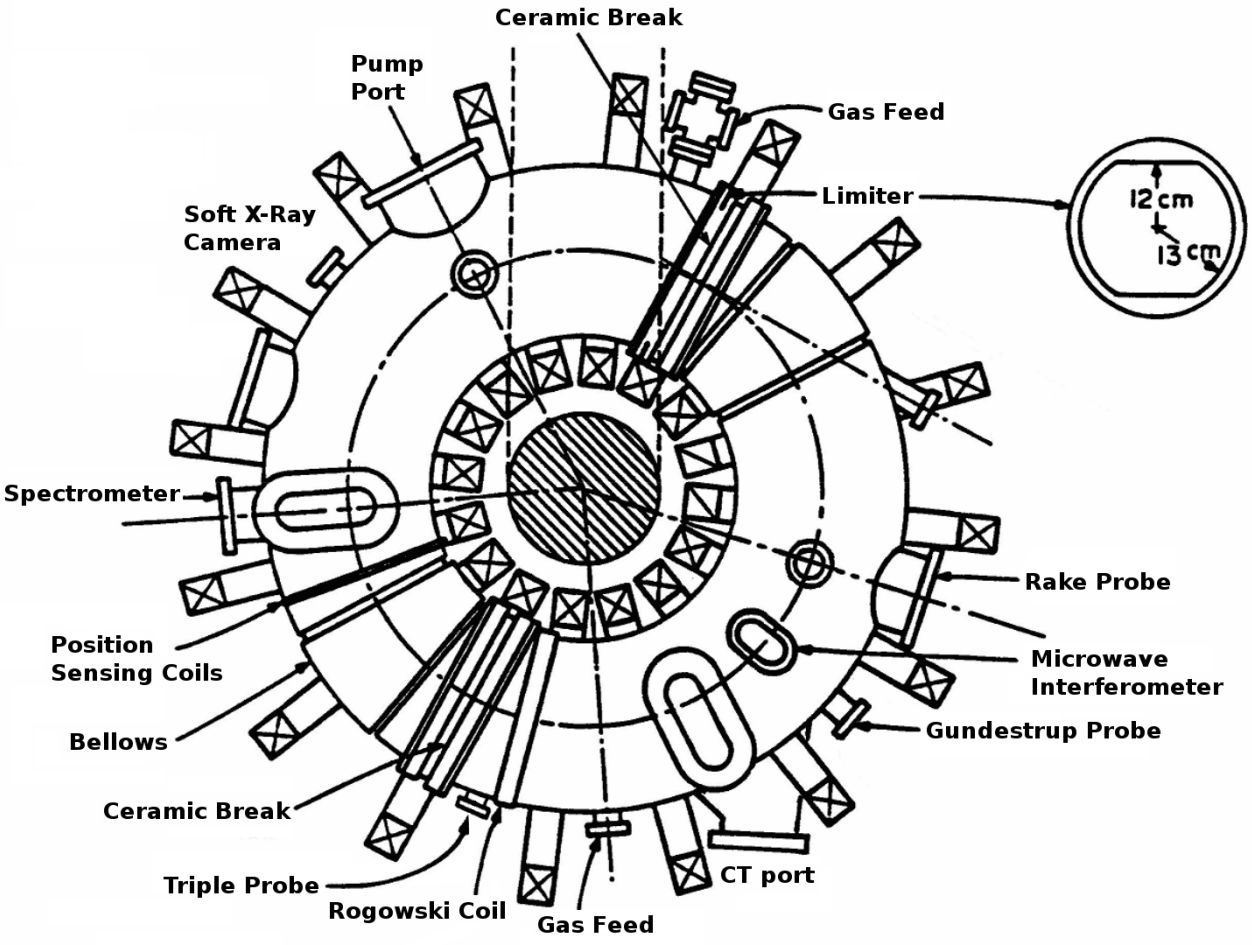

Figure 3.1: Top view of the STOR-M tokamak with diagnostics, other main components and a cross-section of the limiter.

R	Major radius	46 cm
a	Minor radius	12 cm
B_ϕ	Toroidal magnetic field	1 T (max)
I_P	Plasma current	30 - 40 kA
n_e	Average electron density	$(1 \sim 3) \times 10^{13}$ cm^{-3}
T_e	Electron temperature (core)	200 - 300 eV
T_i	Ion temperature	50 - 100 eV
τ_e	Energy confinement time	2 ms
t_d	Discharge duration	40 ms
p_B	Base pressure	1×10^{-7} Torr

Table 3.1: STOR-M and discharge parameters.

The vacuum is provided by a turbomolecular pump with a throughput of 1000 L/s, backed up by a rotary vane pump for rough pumping. The base pressure reached by this system is typically 1×10^{-7} Torr, ensuring a low background of impurities. The working gas for STOR-M is ultra pure hydrogen at a pressure of 1-4 $\times 10^{-4}$ Torr, controlled by a PV-10 piezoelectric valve. Additional to this constant feeding valve there are two valves responsible for up to five gas puffs, variable in amplitude, length and starting time.

3.3 Magnetic Field System

Magnetic fields are necessary to confine, shape and position the plasma inside the vacuum chamber. In contrast to a stellarator, the plasma current, besides external coils, also contributes to the magnetic field configuration. All magnetic fields are created by the discharge of capacitors and are described briefly in the following subsections.

3.3.1 Toroidal Field

16 equidistantly placed coils create a toroidal magnetic field of $B_\phi \approx 1$ T. Each coil consists of nine turns of copper, totalling $N = 144$ turns. The whole assembly is connected in series with a resistance of $R = 13.5$ mΩ and an inductance of $L = 2.06$ mH. The capacitor bank for the toroidal

field, consisting of 22 capacitors, stores up to 360 kJ at 7 kV, but is generally charged up to 4.5 kV during normal operation. Since there is only one discharge stage, the current rises within 6.5 ms to its maximum and decays over 400 ms at a time constant $\tau = \frac{L}{R} \approx 150$ ms, resulting in a decaying magnetic field during the discharge.

3.3.2 Poloidal Field

The poloidal field coils are the primary winding of an iron core transformer with the plasma as secondary winding. Eight turns of a copper busbar induce flux into the iron core placed in the centre of the tokamak. The plasma current is the most common way to ohmically heat the plasma and also responsible for the poloidal magnetic field, twisting the total magnetic field into helical paths around the torus. There are three capacitor banks involved in driving the current: the bias bank (450 V, 20 mF) is usually charged to -100 V to negatively bias the transformer iron core before the discharge and increase the available flux in the iron core. The current ramp-up is realized by the fast bank (450 V, 200 mF), usually charged to 160-180 V, which is superseded when the voltage drops to the level of the slow bank (100 V, 10 F). The slow bank maintains the plasma current and is usually charged to 60-70 V.

3.3.3 Turbulent Heating

The plasma resistivity decreases with increasing temperature, thus limiting the effectiveness of ohmic heating. A pulse of high current with a rise time of 40 μs and length of 100 μs experiences higher resistivity due to skin effects and can increase the total plasma current to 50 kA for a short time. The four windings creating the turbulent heating pulse are powered by a capacitor (5 kV, 1 mF) and switched by an ignitron.

3.3.4 Resonant Magnetic Perturbation

Fluctuations of the magnetic field cause a wide range of phenomena that can affect the plasma confinement. Resonant magnetic perturbations (RMP) are used to control or suppress MHD modes by matching the helicity of the coil configuration creating the RMP field. Figure 3.3 shows the cables mounted on the STOR-M plasma vessel, which is a (m=2, n=1) mode configuration to

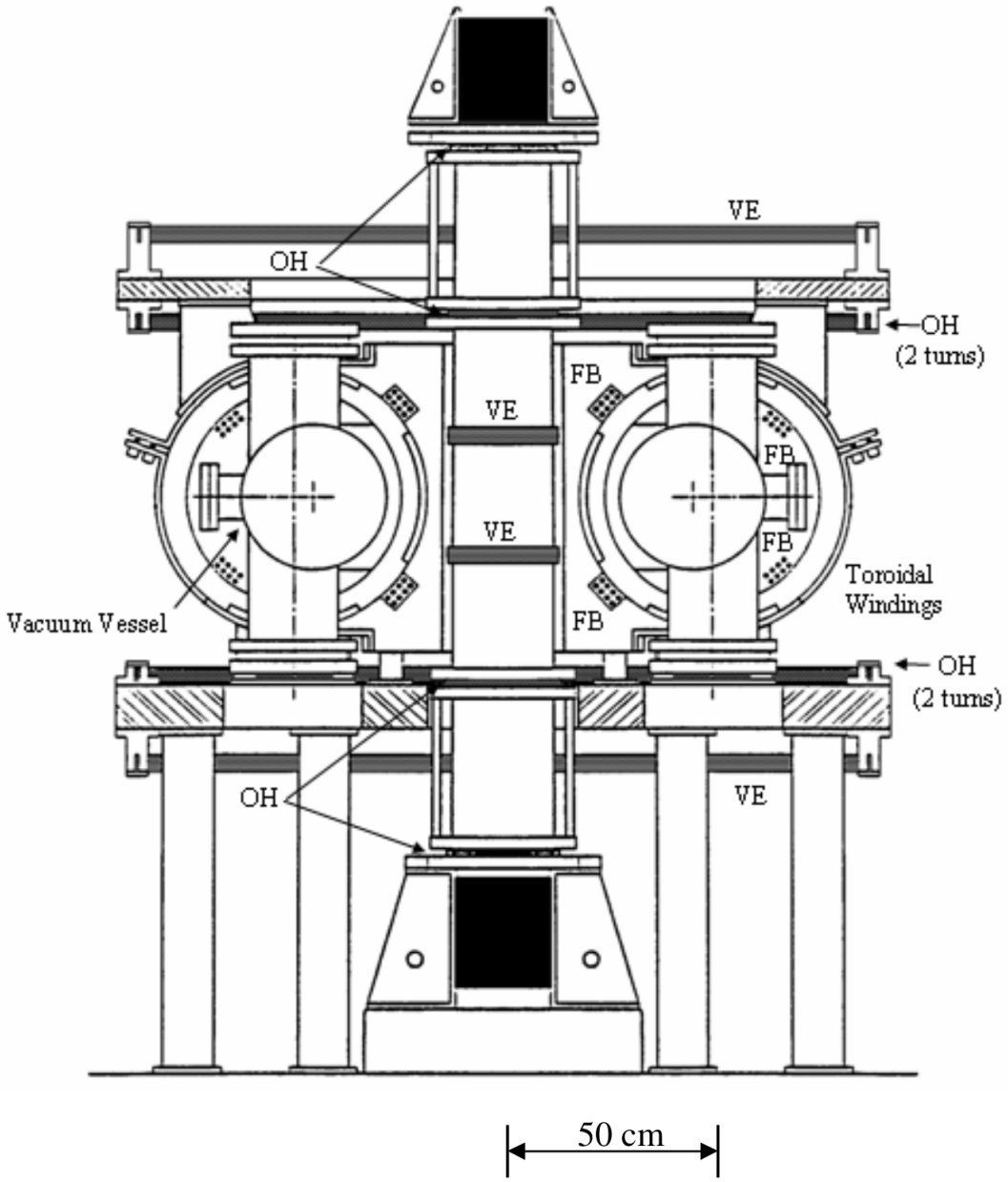

Figure 3.2: Vertical cross-section of STOR-M. Illustrated are the locations of Ohmic Heating (OH) and Vertical Equilibrium (VE) coils and the feedback windings (FB).

interact with magnetic island of the same mode structure. The two helically twisted cables are connected to a fast bank (50 mF, 450 V) and a slow bank (420 mF, 100 V) creating the RMP pulse with an IGBT switch. The pulse length and intensity are variable and double pulses can be realized with an extra circuit.

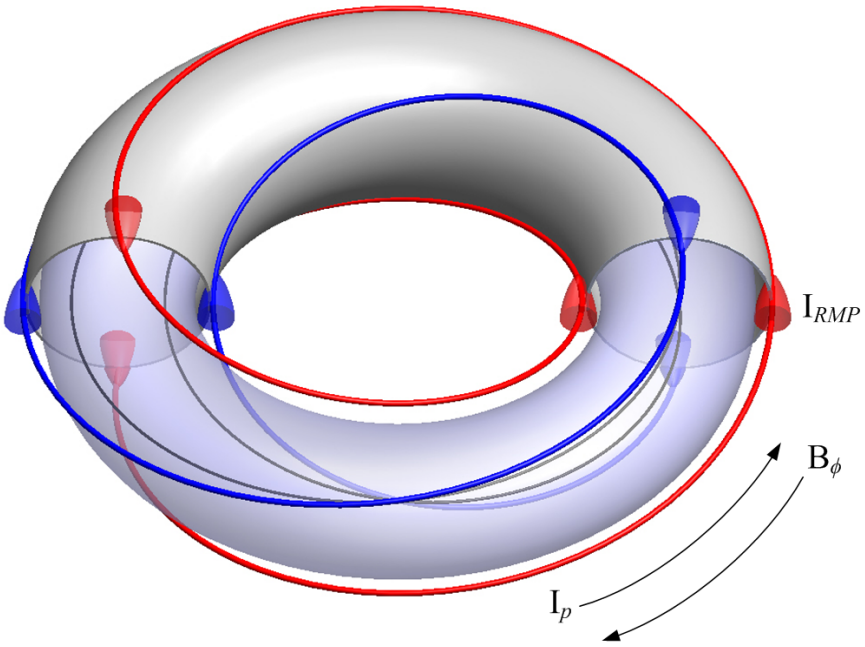

Figure 3.3: RMP coils in (2,1)-configuration around the tokamak with blue and red lines according to the current direction in the cables [27].

3.4 Langmuir Probe

Langmuir probes are a standard plasma diagnostics, since they are cost efficient and versatile. They were first described in the 1920s by *Mott-Smith* and *Langmuir* as a cylindrical electrode immersed into plasma [14]. The electrode can be biased with an AC or DC voltage or left unbiased at the so-called floating potential. Plasma parameters accessible to a Langmuir probe are electron temperature, density and floating potential at a high temporal resolution. Depending on the design and analysis, spatial and temporal correlations of plasma structures can be identified. In some cases even the electron energy distribution (EEDF) can be determined. The usage of Langmuir probes is restricted to low temperature plasma or the edge region of hot plasmas, since they are in contact with the plasma and thus could be damaged or affect the plasma discharge.

The useful bias region reaches from repelling all electrons to repelling all ions and collecting the other species, respectively. The voltage-current-diagram in Figure 3.4 contains the regimes in which a Lamgmuir probe is operated. From the general gas-kinetic theory for an isotropic and homogeneous plasma the flux Γ per area and time can be derived. Combined with the area of the probe and charge of the species, the current I that is collected by an inserted probe is:

$$I = -eA(\Gamma_\mathrm{i} - \Gamma_\mathrm{e}) = -eA\left(\frac{n_\mathrm{i}\overline{v}_\mathrm{i}}{4} - \frac{n_\mathrm{e}\overline{v}_\mathrm{e}}{4}\right), \tag{3.1}$$

where A is the area exposed to the plasma and $\overline{v}_{\mathrm{i,e}}$ is the average ion and electron velocity, respectively. Considering a hydrogen plasma with comparable ion and electron temperature, the electron velocity will be much higher than the ion velocity and any surface experiences a higher net flux of electrons. This higher net flux leads to an accumulation of negative charge on an electrically insulated probe, which will repel enough electrons to achieve zero current. The potential of this equilibrium is called floating potential shown in Figure 3.4 at the zero-crossing. Biasing the probe negatively with respect to the floating potential repels more electrons leading to ion saturation current at which only ions are collected. Increasing the probe potential positively to the floating potential results in repelling the ions and collecting more and more electrons. The end of the exponential increase of the probe current is denoted as plasma potential, at which all electrons are collected. Afterwards geometric effects of the probe are causing a further increase of the electron saturation current.

A Langmuir probe can be operated as one single pin with fixed or sweeping voltage. With a sweeping voltage the full voltage-current diagram can be scanned and thus all properties can be measured at one spacial point. However, the time resolution of the measured quantities is limited by the sweeping duration itself and the need to average over multiple scans. Therefore, fluctuation measurements are carried out at a fixed voltage.

Sheath

Most laboratory plasmas are contained in vacuum chambers and have walls that act as a particle sink, since they have usually a much lower temperature. Differences in the potential between the wall and the plasma are shielded by the plasma in a thin layer called “sheath”. The electrons are rearranging in response to a potential difference, which is called Debye shielding. The sheath forms

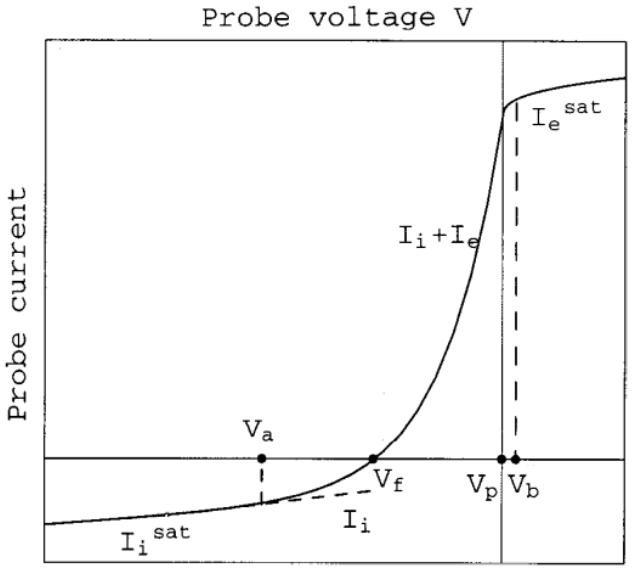

Figure 3.4: Current-Voltage curve of a single Langmuir probe [28].

at walls and all probes, that have a metal surface exposed to the plasma, thus the sheath physics have to be considered when analysing the probe measurements. In the case of a negative bias all electrons are slowed down and reflected, while ions are accelerated towards the probe surface. Due to particle number conservation, the acceleration lowers the density in the sheath region. To avoid a density lower than the electron density, the ions need a minimum velocity before entering the sheath, which is described by the "Bohm sheath criterion". The transition region between plasma continuum and sheath is called presheath and contains a small potential drop, which accelerates the ions to the necessary minimum velocity. Therefore, the density measurement needs to be corrected by a factor, that takes the presheath into account.

3.4.1 Rake Probe

A rake probe is an array of Langmuir probes used to measure the local plasma properties at more than one position simultaneously. In this thesis a 2×8 array rake probe is used, where two 8 pin radial arrays are separated 2.5 mm poloidally. The radial spacing of the pins is 2.5 mm and each pin has a diameter of 0.5 mm with an exposed length of 4 mm. Further dimensions can be seen in Figure 3.5.

The rake probe tips can be used to measure the floating potential or ion saturation current. The floating potential is measured by the circuit with a large input resistance to ensure approximately

zero current (more detail in 4.1). The floating potential level and its fluctuations are linked to the plasma potential. The absence of temperature fluctuations is assumed so that fluctuation of plasma potential and floating potential are identical. The fluctuations of different pins can be used to determine larger structures in the plasma. The ion saturation current is given by:

$$I_{\mathrm{s,ion}} = Cqn_{\mathrm{e}}\sqrt{\frac{k_{\mathrm{B}}T_{\mathrm{e}}}{M}}A_{\mathrm{eff}}, \tag{3.2}$$

where A_{eff} and M are the effective surface area of the probe and the ion mass, respectively. The temperature gradient in the edge and SOL region is sufficiently small for the temperature to be assumed constant. The effective area can be approximated by the tip surface if the dimensions are small compared to the Debye length, which is the case in the STOR-M edge and SOL. The factor C is accounting for the presheath density reduction and depends on the ratio between ion and electron temperature [29]. For most cases, a constant of $C = 0.61$ is used. The ion density fluctuations can be obtained from the ion saturation current if temperature fluctuations are negligible.

The probe head, shown on the left side of Figure 3.5, is made of boron nitride to ensure operation at high temperature (rated melting temperature is 2000 °C) and machinability in contrast to the shaft made from alumina. There are 8×2 holes, spaced 2.5 mm in both directions. The 9 mm long tungsten tips are connected to a grid of single-in-line sockets inside the probe head, which themselves have leads to connect the probe tips to 16 wires. Additionally, there are three wires ending within the shaft close to the tip in order to have noise detecting channels. Since they are inside the shaft and thus shielded from the plasma, they act as antennas. However it was found that the noise level measured by the three extra pins is negligible compared with the signal strength. The mechanical connection between all parts, including the sockets of the probe, is made by Torr Seal epoxy.

3.5 Rogowski Coil

Rogowski coils are used in various places around STOR-M to measure currents, most importantly the plasma current and the currents through magnet coils. Figure 3.6 shows an example of a Rogowski coil with circular cross-section, which picks up the magnetic field around a conductor carrying a changing current with a toroidally wound N-turn coil. The turns are spaced equally around

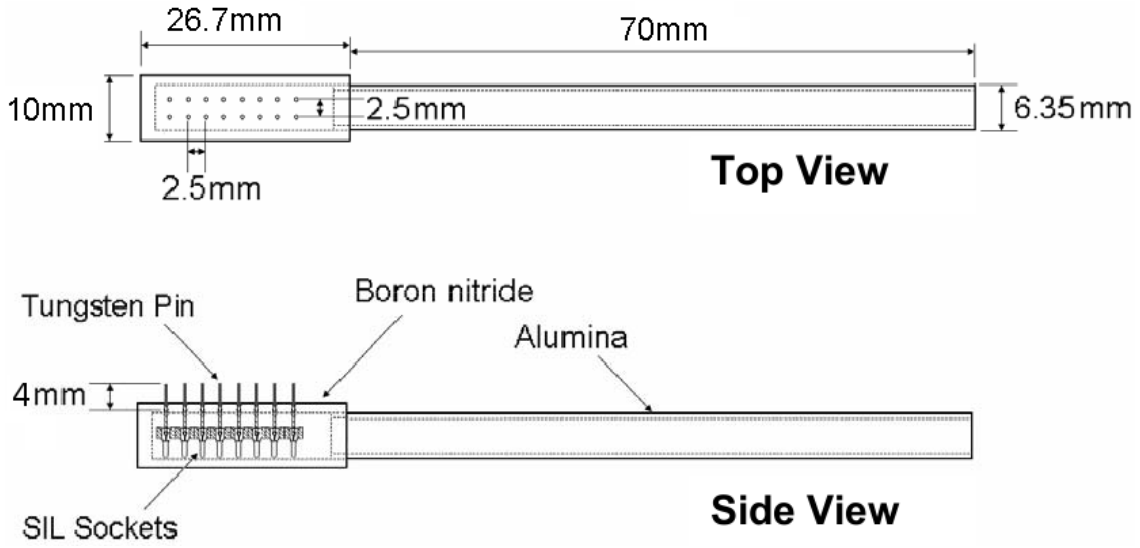

Figure 3.5: 16 pin rake probe, head and shaft, in top and side view (adopted from [30]).

the conductor on a non-magnetic ring. The voltage V_{RC} that is picked up is proportional to the number of turns N and the change of the magnetic flux Φ.

$$V_{\mathrm{RC}} = -N\frac{d\Phi}{dt} \tag{3.3}$$

To calculate the current, the magnetic flux is needed as a first step, found by integration of V_{RC} over time. This yields the magnetic flux as a function of time, to which Ampere's law can be applied:

$$I = \oint_c \vec{H}\cdot\vec{dl} = \frac{\phi}{A\mu_0}2\pi R_{\mathrm{R}} = -\frac{2\pi R_{\mathrm{R}}}{\mu_0 NA}\int V_{\mathrm{RC}}dt, \tag{3.4}$$

where H is the magnetic field intensity, μ_0 the permeability of vacuum, R_{R} the major radius and A the area encircled by one turn. Rogowski coils can be installed easily without affecting the circuit and because of the absence of an iron core there are no non-linear effects or saturation. They are also able to measure currents with high temporal resolution due to their low inductance.

3.6 Loop Voltage

The loop voltage is one of the main plasma parameters and Figure 3.7 shows the corresponding circuit. It contains essential information about the resistance of the plasma and thus the level of impurities and plasma temperature. It can be measured by a single wire in a toroidal loop parallel

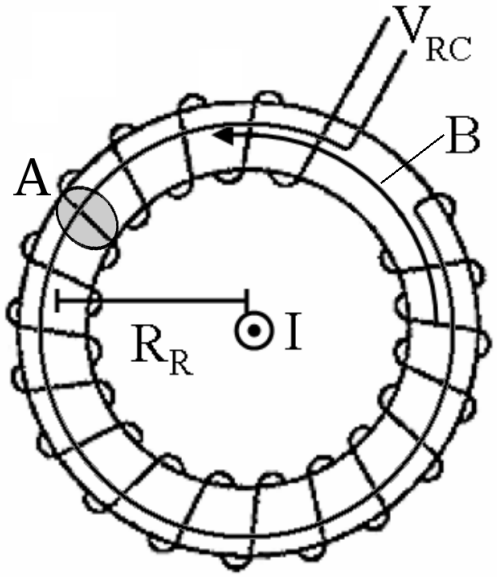

Figure 3.6: Rogowski coil with magnetic field, created by the current in the middle (adopted from [30]).

to the plasma current. The loop voltage V_l consists of a resistive and inductive part:

$$V_\mathrm{l} = R_\mathrm{P} I_\mathrm{P} + \frac{d}{dt}(L_\mathrm{P} I_\mathrm{P}), \tag{3.5}$$

where R_P is the resistance of the plasma, I_P the plasma current and L_P the plasma inductance. Treating the plasma as a conductor with a certain length and cross-section an average resistivity η parallel to the magnetic field can be related to the resistance

$$R_\mathrm{P} = \frac{2\eta R_0}{a^2}. \tag{3.6}$$

The plasma can be approximated as a circular loop for which the inductance is

$$L_\mathrm{P} = \mu_0 R \left[\ln\left(\frac{8R}{a}\right) + \frac{l_\mathrm{i}}{2} - 2 \right], \tag{3.7}$$

where a is the minor radius and l_i is the internal plasma inductance parameter, which depends on the plasma current density profile. The internal plasma inductance parameter is defined as:

$$l_\mathrm{i} = \frac{\overline{B_\theta^2}}{B_\theta^2(a)}, \tag{3.8}$$

where B_θ is the poloidal component of the magnetic field. Depending on the current profile in a poloidal cross-section, l_i ranges from zero for a pure skin current to 0.5 for a uniform current density. Centrally peaked profiles result in $l_i \geq 1$.

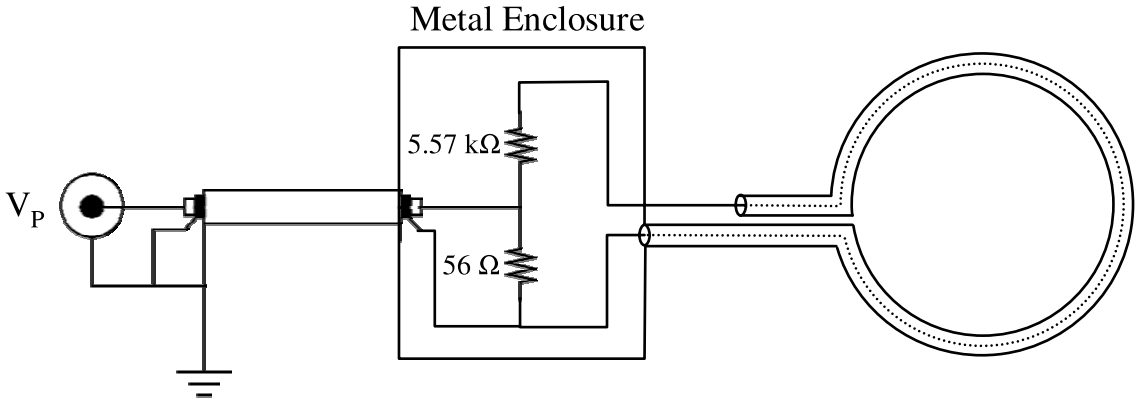

Figure 3.7: Loop voltage measurement schematic and circuit [31].

3.6.1 Spitzer Temperature

After the current ramp-up the change of current is very small during the flat-top phase of the discharge, thus equation 3.5 can be simplified to $V_\mathrm{l} \approx R_\mathrm{p} I_\mathrm{p}$. The neoclassical resistivity η_nc takes trapped electrons into account, which increases the resistance as follows:

$$\eta_\mathrm{nc} = \frac{\eta_S}{1 - 1.95\sqrt{\varepsilon} + 0.95\varepsilon} \tag{3.9}$$

with the inverse aspect ratio $\varepsilon = a/R$ (for $\varepsilon \approx 0.3$ in STOR-M, $\eta_\mathrm{nc} \approx 3.5\eta_\mathrm{S}$) and η_S is the Spitzer resistivity based on classical coulomb collision theory:

$$\eta_\mathrm{S} = 1.65 \times 10^{-9} \frac{Z_\mathrm{eff} \ln\Lambda}{T_\mathrm{e}^{3/2}}\ \Omega\mathrm{m}, \tag{3.10}$$

where the unit for the electron temperature is eV and $Z_\mathrm{eff} \approx 1.5$ is the effective ion charge number, which depends on the level of impurities. $\ln\Lambda$ is the Coulomb logarithm, which can be calculated as follows:

$$\Lambda = 12\pi n_\mathrm{e} \left(\frac{\varepsilon_0 T_\mathrm{e}}{n_\mathrm{e} e^2} \right)^{3/2}. \tag{3.11}$$

Λ is insensitive to the temperature and density and can be estimated from typical STOR-M discharge parameters ($n_\mathrm{e} = 5 \times 10^{12}$ cm^{-3}, $T_\mathrm{e} = 220$ eV) to about 17. With the resistivity only depending on the temperature and the total plasma resistance, which is given by the loop voltage and plasma current, the average electron temperature can be approximated by taking the plasma column dimensions as the conductor length and radius. This leads to a plasma temperature of:

$$T_\mathrm{e}(\mathrm{eV}) = \left(\frac{0.0116 I_\mathrm{p} R}{V_\mathrm{l} a^2} \right)^{2/3}. \tag{3.12}$$

Iterations can be made to use the calculated temperature in equation 3.12 to recalculate Λ in equation 3.11, so the next calculation of the temperature in equation 3.12 is more accurate. Typical discharge conditions in STOR-M ($I_p \approx 25$ kA, $V_l \approx 3$ V) result in a temperature of about 200 eV.

3.7 Position Sensing Coils

The vertical and horizontal position of the plasma column must be measured accurately and fast enough to provide a good input for the feedback position control system. This ensures a good plasma quality by minimizing the contact between limiter and plasma. A set of six coils measures the magnetic field created by the plasma to determine the plasma position. The configuration shown in Figure 3.8 consists of four poloidally separated coils, measuring the poloidal magnetic B_θ field at the same toroidal location. Additionally, two coils above and below the plasma measure the radial magnetic field B_r. All of the coils are mounted outside the vacuum chamber.

To account for unwanted signals, which are arising from background signals also present in absence of the plasma, due to external coils, a compensation circuit is used. Rogowski coils determine the waveform of magnetic fields produced by the misalignment and imperfection of the toroidal field coils and the sensing coils. This stray field pick-up is compensated for by the circuit while other contributions i.e. the Ohmic heating, leakage magnetic field are sufficiently small.

3.8 Mirnov Coils

Mirnov coils are modified Rogowski coils with variable winding density, practically covering only a fraction of the full toroidal turn. This makes it possible to detect different modes of fluctuation depending on how many Mirnov coils are used along a certain direction. Assuming harmonic oscillations the poloidal magnetic field can be expressed by a Fourier expansion:

$$B_\theta(\theta) = B_{\theta,0} + \sum_{m=1}^{\infty} \left[A_m \cos(m\theta) + B_m \sin(m\theta)\right]. \tag{3.13}$$

$B_{\theta,0}$ is the unperturbed poloidal field and the following sum contains all modes of fluctuations of the poloidal field. This expansion can also be done along the toroidal angle ϕ of the torus, replacing the poloidal mode number m by the toroidal mode number n. STOR-M is equipped with a Mirnov

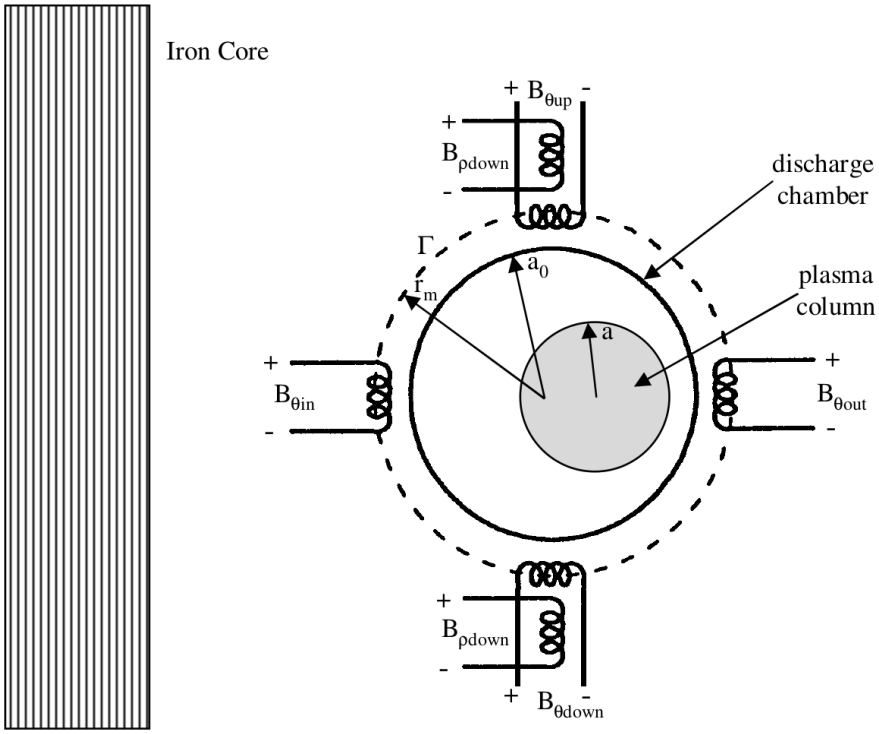

Figure 3.8: Coils measuring poloidal and radial magnetic field to deduce plasma position [31].

coil array consisting of 12 individual coils around a poloidal cross-section and four coils at the outboard side along the toroidal direction. Thus, poloidal mode numbers up to $m = 6$ and toroidal mode numbers up to $n = 2$ can be resolved. Signals from different toroidal positions have to be corrected, if the chamber thickness differs, since the signal experiences a delay traveling through the metal chamber.

3.9 Interferometer

A standard method of density measurement on laboratory plasmas is the microwave interferometer. A diagram of the interferometer is shown in Figure 3.9, where important components along the microwave path are marked. STOR-M uses a 76 GHz ($\lambda = 4$ mm) cavity-stabilized Gunn diode to generate microwaves, which are divided into two reference paths ($E_{r1,r2}$) and one path passing through the plasma (E_s). Electromagnetic waves travel at different velocities depending on the plasma density. Thus the phase shift between reference and plasma path can be used to deduce the line averaged electron density. The maximum density that can propagate through the plasma is

called the cut-off density, n_{cut}, a plasma with higher density reflects the incoming wave. For the 76 Ghz microwave used at STOR-M the cut-off density is

$$n_{\text{cut}} = \frac{\omega^2 \varepsilon_0 m}{e^2} \approx 7 \times 10^{19}\ \text{m}^{-3}, \tag{3.14}$$

where m is the electron mass, ε_0 is the dielectric constant and ω is the angular frequency of the microwave. The path of one microwave beam leads vertically through the centre of the plasma, thus the measured phase shift $\Delta\phi$ relates to the density profile as follows:

$$\Delta\phi = \frac{2\pi}{\lambda} \int (n(x) - 1) dx = \frac{2\pi}{\lambda} \int_{-a}^{a} \left(1 - \sqrt{1 - \frac{n(x)}{n_{\text{cut}}}} \right) dx, \tag{3.15}$$

where λ is the wavelength of the microwave and $n(x)$ is the density profile. Integrating an assumed or measured density profile, assuming $\frac{n(x)}{n_{\text{cut}}} \ll 1$, leads to the central line averaged density :

$$\overline{n}_{\text{e}} = \frac{1}{2a} \int_{-a}^{a} n(x) dx = \frac{\Delta\phi}{2\pi} \frac{\lambda}{a} n_{\text{cut}}. \tag{3.16}$$

After exiting the plasma, the microwave signal E_{s} passes through an E-H tuner and is split into two components ($E_{s1,s2}$), in order to mix them with the two reference paths in hybrid tees. Four silicon point-contact diodes measure the microwave signals, which are then transformed into voltage signals by buffer amplifiers. With correctly adjusted phases and amplitudes, the output signals are 90° phase shifted and read:

$$V_1 = K_1 \sin\Delta\phi \tag{3.17}$$

$$V_2 = K_2 \cos\Delta\phi, \tag{3.18}$$

where $K_{1,2}$ are amplification constants. The phase shift makes sure that an increase or decrease of plasma density can be distinguished at any time. Counting the zero transitions leads to the line averaged density.

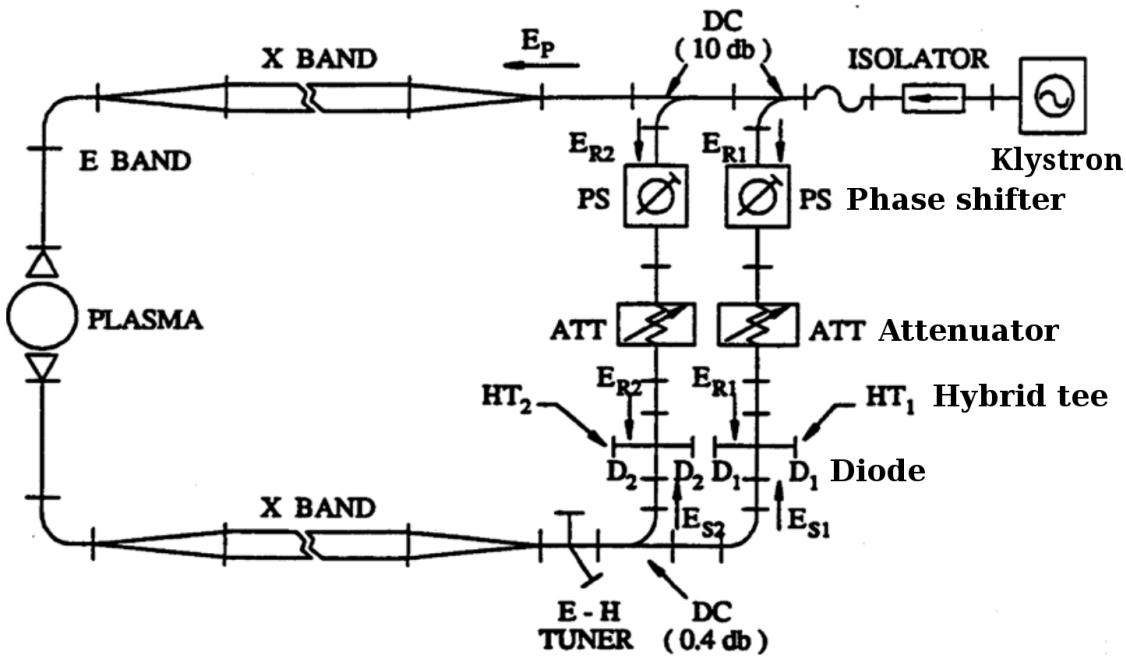

Figure 3.9: 4 mm interferometer path with important components indicated along the microwave path [32].

CHAPTER 4

DATA ACQUISITION AND SIGNAL PROCESSING

Each pin of the rake probe can either be used for floating potential or ion saturation current measurements. A high sampling rate is needed to ensure that fluctuations up to 50 kHz in both types of measurements can be resolved. The signal processing and analysis was done with MATLAB. Major analysis techniques were programmed, benchmarked and compared with MATLAB routines, if they already existed, with the exeption of the fast Fourier transform.

4.1 Data Acquisition

The data acquisition consists of two parts for each operation modes. Different circuits are used for ion saturation and floating potential measurements. The floating potential measurements require zero current and a short cable to minimize its capacitance. A rack right next to the tokamak holds two eight-channel cable drivers. The input stage consists of a voltage divider which makes the voltage accessible to the cable driver input and the digitizers. The core piece of the driver is the LM6181 current feedback amplifier, which operates at unity gain with 100 MHz bandwidth. The 50 Ω output resistor matches the coax cable going to the data acquisition system. Figure 4.1 shows the cable driver with input and output resistors.

To collect the ion saturation current, the probe tip needs to be biased negatively with respect to the plasma or floating potential. However, using this reference requires contact to the plasma and collecting electron current in the same order as the ion saturation current. Alternatively, the bias voltage can be applied with ground reference to the plasma chamber. Since the plasma potential can be negative in respect to the chamber, the applied voltage needs to be more negative to compensate for this difference, otherwise the pins collect electron current. The combination of a variac and a rectifier can supply up to -180 V. However, -100 V bias voltage was used during most

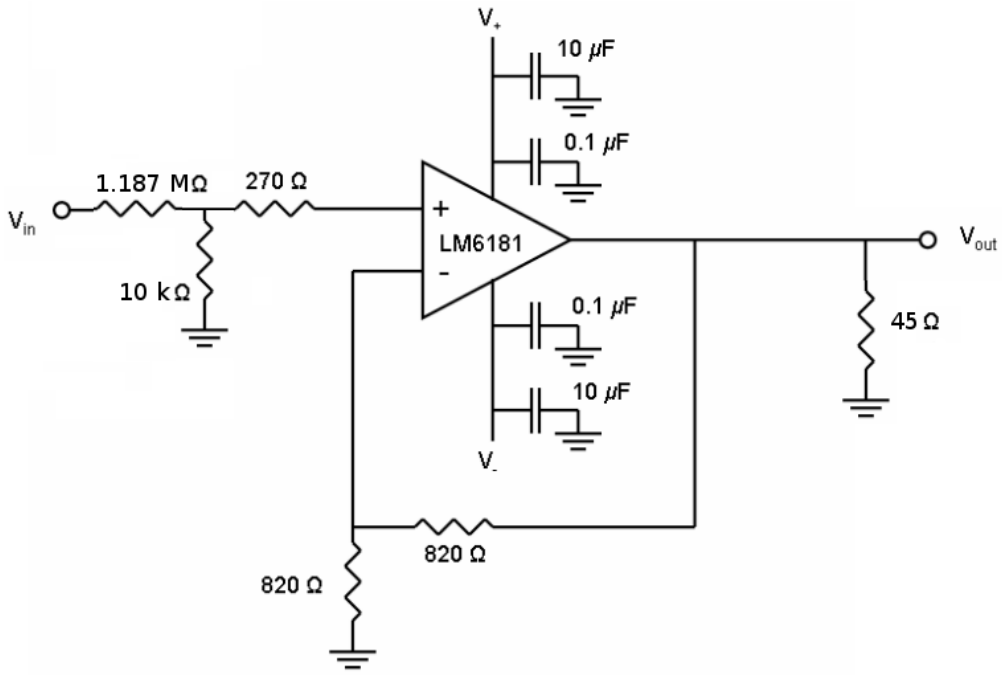

Figure 4.1: The circuit to acquire floating potential consists of a high resistance voltage divider and a cable driver.

experiments. Two capacitors were used as a buffer to stabilize the bias voltage. The ion saturation current flows through a 0.25 Ω current sensing resistor connected in series with the power supply and the probe pins. The voltage drop across the resistor is measured and leads to the ion saturation current. A circuit schematic is shown in Figure 4.2. The voltage output is connected to an isolation amplifier, because the current sensing resistor is at the biased potential.

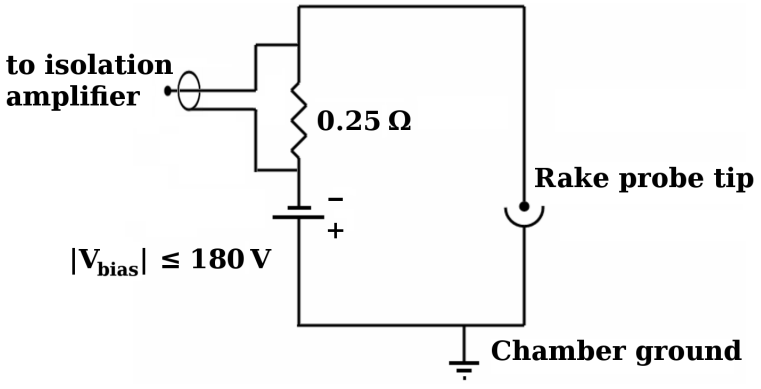

Figure 4.2: Schematic drawing for ion saturation current collection.

The final stage for both types of measurements are National Instrument BNC-2110 or BNC-2120 terminal blocks. They are each connected by a 100-pin shielded cable to a National Instru-

ments PCI-6133 card, which can simultaneously sample 8 analog signals with a sampling rate of 2.5 megasamples per second (MS/s). Each card has a memory of 16 MS with a resolution of 14 bit. A Labview program provides the communication between DAQ and PC, setting the trigger, sampling rate and number of samples. The maximum input voltage is adjustable up to ± 10 V, always applying the 14-bit resolution to the set input range. All measurements were conducted with 1 MHz sampling rate and the input range is adjusted to the signal levels, to achieve maximum amplitude resolution.

4.2 Signal Processing

Fluctuating plasma quantities contain important information in the spectral domain. Depending on the processes causing the fluctuations in plasma potential or density, different techniques have to be applied to extract / identify them. The Fourier transformation gives access to the frequency domain of the collected data. Signals at different positions can be compared in time and frequency domains. The techniques used are explained briefly below.

Fourier Transform

The concept of Fourier transform (FT) is named after *Joseph Fourier*, who developed this method in the early 1800's in the study on heat conduction. Generally, FT serves as a bridge between the time domain and the frequency domain and led to the development of transforms in other domains. Various methods based on FT give powerful tools to characterize fluctuating signals. There are three types of domain signals, nonperiodic, periodic and discrete. The continuous FT is used to decompose an algebraic waveform into an infinite sum of harmonic oscillations. The opposite calculation from the frequencies domain to the time domain is called inverse Fourier transform. Together the pair of FT functions can be written as

$$X(f) = \int_{-\infty}^{\infty} x(t) e^{-i2\pi ft} dt \tag{4.1}$$

$$x(t) = \int_{-\infty}^{\infty} X(f) e^{i2\pi ft} df, \tag{4.2}$$

where $X(f)$ and $x(t)$ are the waveforms in the frequency and time domain, respectively. For digitized data a discrete version of the FT has to be employed, which introduces certain constraints

due to the sampling rate and finite intervals. In the discrete FT, the integrals are replaced by a summation, resulting in the following form

$$X(j) = \frac{1}{N}\sum_{k=0}^{N-1} x(k)e^{-i2\pi jk/N}, \quad j = 0,1,2...,N-1 \tag{4.3}$$

$$x(k) = \sum_{j=0}^{N-1} X(j)e^{i2\pi jk/N}, \quad k = 0,1,2...,N-1 \tag{4.4}$$

where j and k are the frequency and time index, respectively. The total number of samples is N and poses a lower frequency limit, while the sampling rate t_s sets the limit for resolving high frequencies [33].

Using equation 4.3 for the actual computation would require N^2 complex calculations and thus quickly exceed computation capabilities of regular computers. The numbers of discrete FT computations can be drastically reduced by using the fast Fourier transform (FFT) developed by *James Cooley* and *John Tukey* [34].

Auto/Cross-correlation

Folding a function or discrete data sets with a reference function or data, reveals how similar the signals are and if it contains propagating features. Comparing a data set with itself tests for repeating patterns. The implementation for discrete data follows

$$R(m) = \sum_{n=-\infty}^{\infty} X(n)\cdot Y(n-m), \tag{4.5}$$

where the two signals $X(m) = x(t_m)$ and $Y(m) = y(t_m)$ are discrete data points collected at times $t_m = m\Delta t_s = m/f_s$. For auto-correlation, zero time delay will give the maximum value and then decline, defining the correlation time of the signal(s). In case of a propagating wave the cross-correlation will have a maximum at the time the wave needs to travel between the two positions. If the maximum is shifted towards a positive time lag $m \geq 0$, the second signal $X(n-m)$ uses a smaller argument, thus being shifted to an earlier time, representing a wave propagating direction from Y to X. Unless otherwise mentioned, the reference ($X(n)$) channel is always the innermost pin of the rake probe, which means that a positive time lag indicates a radially inwards propagation. With the velocity of a structure or wave, the physical size of a coherent structure can be found by combining velocity and auto-correlation time. The decay of the maximum cross-correlation

value with increasing distance can also be used, but needs to be corrected for different fluctuation amplitudes.

Power Spectrum and Coherence

Performing a Fourier transformation on the correlation function is mathematically equivalent to multiplying the individually fourier transformed signal in the following way

$$P_{XY}(f) = R(f) = X^*(f) \cdot Y(f), \tag{4.6}$$

where $X^*(f)$ denotes the complex conjugate of the Fourier transformation. If there is a propagating wave travelling a distance Δx, the phase of the involved frequency components will change/rotate by an amount $\Delta\Phi$ within that distance. Two waves can have the same frequency, but independent causes. Their phase difference will be randomly distributed if they are not related. Adding up different realizations of complex valued power spectra will result in a measure of how connected each frequency of the spectrum is. The coherence is defined by

$$C_{XY}(f) = \frac{\mid \langle P_{XY}(f) \rangle \mid}{\sqrt{\langle P_{XX}(f) \rangle \langle P_{YY}(f) \rangle}}, \tag{4.7}$$

where $\langle ... \rangle$ denotes the average over k similar realizations:

$$\langle P_{XY}(f) \rangle = \frac{1}{k} \sum_k \mid P^k_{XY}(f) \mid e^{i\Delta\Phi^k_{XY}(f)} \tag{4.8}$$

$$\langle P_{XX}(f) \rangle = \frac{1}{k} \sum_k P^k_{XX}(f) \tag{4.9}$$

$$\langle P_{YY}(f) \rangle = \frac{1}{k} \sum_k P^k_{YY}(f), \tag{4.10}$$

where k independent ensembles of cross-power spectra are averaged with their phase information. The power spectrum shows how much power the signal has per unit frequency, but it will not account for differences in the phase of signals. If two signals at a certain frequency are not coherent they will have a random phase differences and give zero when averaged over many ensembles. Coherent signals on the other hand will have a constant phase difference, resulting in a finite value after averaging. So the coherence can show, if there is one connected oscillation in two channels or only random oscillations.

Probability Density Function

The probability density function (PDF) characterizes the amplitude distribution of a fluctuating signal by binning the values of the time series in equi-amplitude intervals. For experimental data the PDF is a discrete function and the probability to find a certain value x_i in the interval i is:

$$P(x_i) = \frac{N_i}{N}, \tag{4.11}$$

where N_i is the number of events in the interval i and N is the total number of data points in the regarded time window. To make different fluctuation levels more comparable, the intervals are multiplied by the standard deviation ($PDF = P(x_i)\sigma$) and the amplitude is expressed in standard deviations (e.g. $I_{\mathrm{sat}}(\sigma) = I_{\mathrm{sat}}/\sigma$).

The standardized central moments are used to characterize the PDF and are defined as:

$$m_k = \sum_n \frac{(x_n - \langle x \rangle)^k}{\sigma^k}, \tag{4.12}$$

where $\langle x \rangle$ is the mean value of the time series and k the order of the moment. The first moment is zero by definition and the second moment gives 1, since the nominator of equation 4.12 with $k = 2$ is the definition of the standard deviation. The third moment is called skewness S and indicates if the time series is Gaussian ($S = 0$) or if the PDF is asymmetric. Large positive peaks with smaller frequent negative peaks will result in a positive skewness and vice versa. The fourth moment is called Kurtosis K, which indicates if the PDF is dominated by infrequent, large deviations ($K > 3$) or by smaller deviations ($K < 3$). Since a Gaussian distribution yields $K = 3$, sometimes the definition of the Kurtosis is subtracted by 3.

CHAPTER 5

EXPERIMENTAL RESULTS

5.1 Introduction

5.2 Normal Ohmic Discharges in STOR-M

Normal ohmic discharges in STOR-M with reproducible plasma conditions are used as a reference. Those discharges include the flat-top phase, referring to the almost flat plasma current. The discharge in STOR-M begins with a seed plasma created by a hot filament and application of an RF field 1 ms before the toroidal electric field. After the initial breakdown the seed electrons are accelerated and create more electrons by collisional ionization of neutral particles. Furthermore, this pre-ionization increases the reproducibility of the initial breakdown and subsequently for the whole discharge. The current ramp up phase lasts about 10 ms and is driven by the fast Ohmic capacitor bank, followed by the slow bank providing current drive for the flat-top phase. Ideally all plasma parameters are constant during this phase, however there is usually a slow variation of the plasma current and plasma position, which is controlled by a feedback system. Since the toroidal magnetic field is powered by a single stage capacitor bank, the toroidal magnetic field declines as well. The base pressure of the vacuum chamber and four programmable gas puffs determine the plasma density and its evolution during the discharge. A fifth strong gas puff terminates the discharge usually at 40 ms to avoid an excess of runaway electrons, which could damage the wall and internal probes.

The waveforms of a typical plasma discharge is shown in Figure 5.1 with the basic plasma diagnostic equipment recording plasma current (I_P), loop voltage (V_l), central line averaged density ($\overline{n}_e$), horizontal plasma position (ΔH), intensity of H_α emission and gas puffing voltage.

Indicators for a change of the confinement properties are the temperature and the confinement

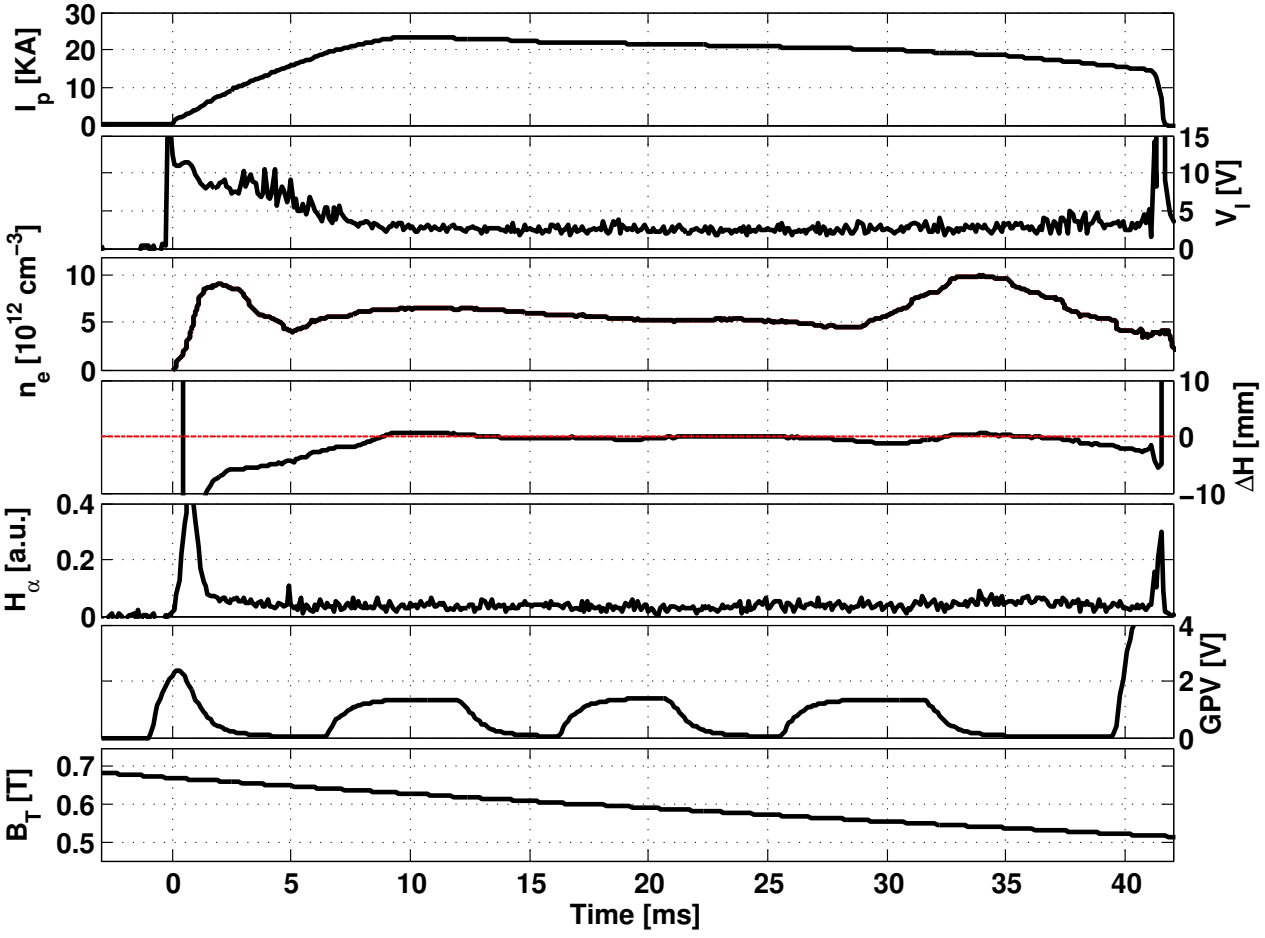

Figure 5.1: Typical ohmic discharge parameters for shot 252079.

time of the plasma. Since the resistivity is dependent on the electron temperature, the neoclassical resistivity can give an estimate for the average electron temperature T_e. How long the energy is stored in the plasma is described by the energy confinement time τ_e. The energy content of the plasma is calculated by the temperature and density of the plasma, i.e. the plasma pressure. The only presently installed heating source is ohmic heating by the plasma current. The global energy confinement time during the flat-top is calculated through $\tau_e = \frac{nk_B T(2\pi R\pi a^2)}{I_P V_L}$. Figure 5.2 shows T_e and τ_e for a typical ohmic discharge, where the electron temperature during the equilibrium phase reaches $T_e \approx 220$ eV and the energy confinement time is in the order of $\tau_e \approx 1$ ms.

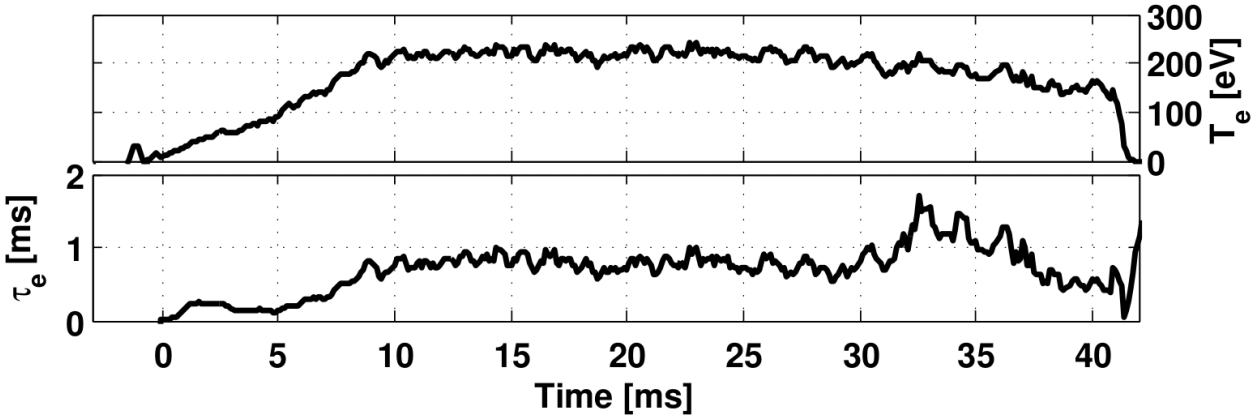

Figure 5.2: Average electron temperature T_e and energy confinement time τ_e waveforms during an ohmic discharge.

Typically, profiles of ion saturation current and floating potential are realized by configuring a number of probe tips to either type of measurement. The radial position of the probe is changed to different locations to acquire a full profile. Rather than slowly increasing towards the centre, the position is changed "randomly" to all desired locations to average out the errors due to slowly changing discharge conditions. Error bars are estimated by the standard deviation of all measured values at a particular position.

5.2.1 Floating Potential

The first part of the experimental results relate to floating potential measurements using rake probes, aiming to characterize spatial and frequency features of the fluctuations. Reproducible plasma conditions are used to create a profile that covers a wide range of positions from the edge region to the SOL.

A raw signal of the floating potential is shown in Figure 5.3, with an averaged signal overlaid. In the edge and SOL region the mean value is typically between 0-30 V, but in contact with plasma it can drop to larger negative values as will be seen in the following profiles. The floating potential signal is dominated by large amplitude fluctuations, which can be characterized by the root-mean-square (RMS) for its amplitude.

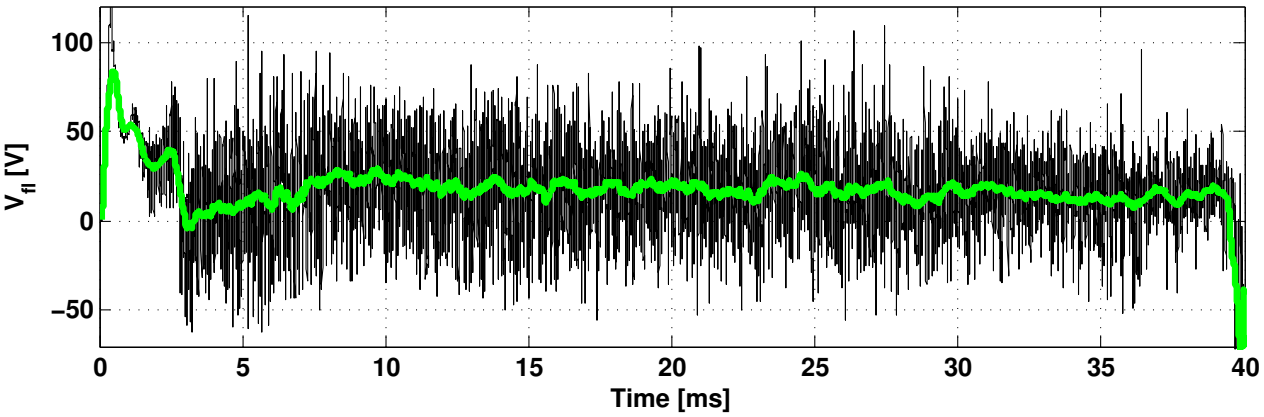

Figure 5.3: Raw Signal in black with 500 μs running average in green at $r = 11.25$ cm, shot 252078.

To identify moving structures in the plasma and determine their size and velocity, the cross-correlation is calculated as a first step. A 4 ms window, i.e. a data segment with a length of 4 ms during the flat-top phase, was used for the calculation in Figure 5.4, where the cross-correlation of the floating potential fluctuations is shown with the first pin as the reference signal. The cross-correlation can be used to estimate the phase velocity of a moving structure by the time shift of the maximum. The inset zooms in on the maxima of the cross-correlation waveform and shows a clear shift starting after a distance of $\Delta r = 0.5$ cm. Averaging over the time shift and distance of the last four cross-correlations, a radial propagation velocity of $v_{rad} = 5.9$ km/s can be estimated. Based on the discussion in Section 4.2, a positive delay on the cross-correlation indicates a propagation from Y (outer probe pin) to X (inner probe pin). In other words, the fluctuation propagates inwards. However, the construction of velocity profiles is unpractical, since the velocity estimate is an average value for the whole length of the rake probe. Another characteristic length can be estimated by the e-fold decline of the maximum values of the correlation, however a different normalization might be needed to account for changing fluctuation amplitudes. The normalization here is done by the auto-power maximum of the first pin.

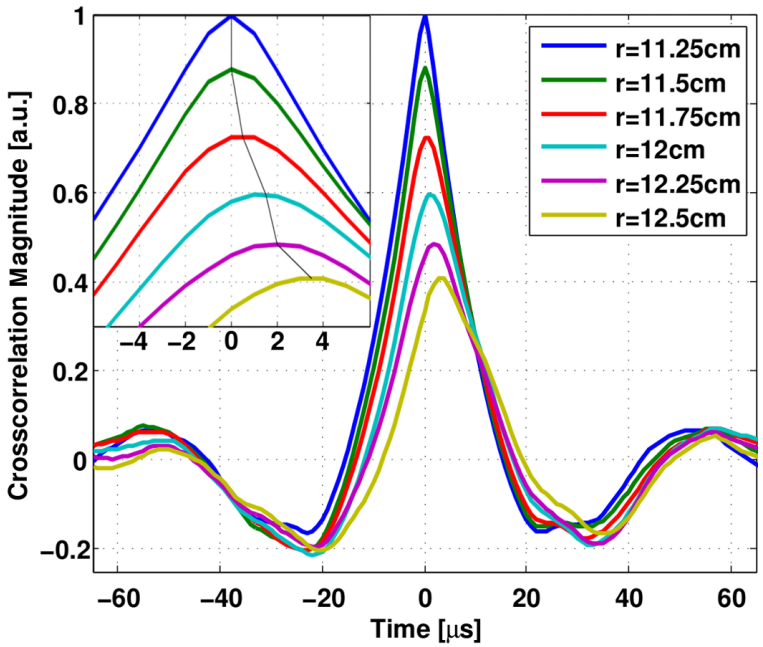

Figure 5.4: Cross-correlation of the floating potential fluctuation signal, with the first pin at $r = 11.25$ cm as reference, with inset zoomed at the maxima of the correlation functions.

Figure 5.5 shows the auto-power spectrum of the floating potential fluctuations during a part of the flat-top phase of the plasma (t = 10-21 ms). The highest amplitude of fluctuations is clearly in the low frequency range, where the amplitude decreases in the radial direction, recognizable by the signals of different rake probe pins. Above $\approx$ 30-40 kHz a roughly f^{-1} behaviour is visible, which declines faster with power law of f^{-3} to f^{-4} and at a similar level for all positions after $f \approx 100$ kHz. In Figure 5.5 the average auto-power spectra above 200 kHz was fitted by a power law, which yields a power dependence of $P \sim f^{-3.18}$.

5.2.2 Ion Saturation Current

The profile of the ion saturation current was measured during a series of similar discharges. Electron and ion temperature were not measured simultaneously, but similar experiments at STOR-M show an increase of the temperature on the order of 10-30 eV from the SOL to the edge region. Assuming an average temperature of 20 eV leads to a steepening of the calculated density profile, but the real temperature profile for the presented discharges is not known. Thus, the error may be affected by $\sqrt{T_e(r)}$ in the density estimation. If not otherwise mentioned the density is used for all figures and calculations with the assumed temperature of $T_e = 20$ eV. For spectral analysis and

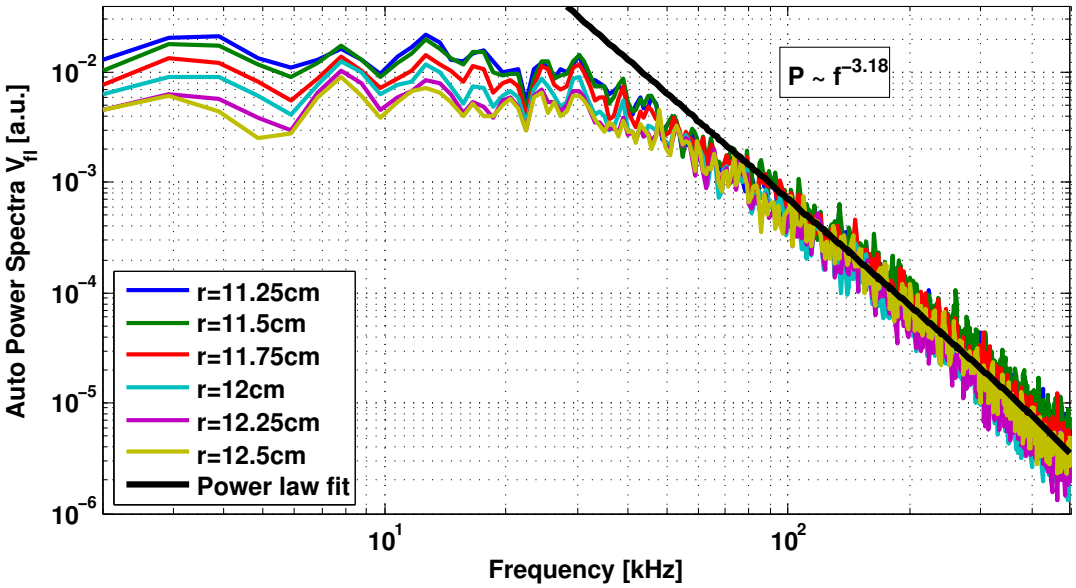

Figure 5.5: Autopower spectrum of six floating potential fluctuation signals with power law fit for the averaged signal above 200 kHz, shot 247614.

higher order momenta the absolute value of the density is unimportant.

The general waveforms of the plasma density in the edge and SOL region follow the line averaged plasma density waveform measured by the interferometer. Figure 5.6 shows the cross-correlation of the plasma density fluctuations for a 4 ms segment and the raw density signal in a short time frame over 200 μs. Auto- and cross-correlation of the plasma density fluctuation signals can be interpreted similar to the floating potential fluctuations, characterizing the decorrelation time and velocities of moving structures. The shift of the maximum point in the cross-correlation for the more distant pins indicates that the density fluctuations also propagate radially inwards. The waveforms show asymmetries in width of the correlation peak and there is a smaller negative peak only on the left side of the positive main peak. The asymmetric width can explain the shape of the plasma density fluctuations shown in Figure 5.6 (b). The rise of the density is short and steep with a slower decay afterwards, especially for the inner pins. For the most positions in the edge and SOL region the plasma density shows positive peaks on top of a background level. If the peaks surpass a defined level, normalized to the standard deviation of the signal, they are called intermittent transport events or blobs, while negative spikes are called holes. To characterize the peaks the skewness is used and more detailed discussions will follow.

Figure 5.7 shows the spectral density of the auto-power for ion saturation current fluctuations.

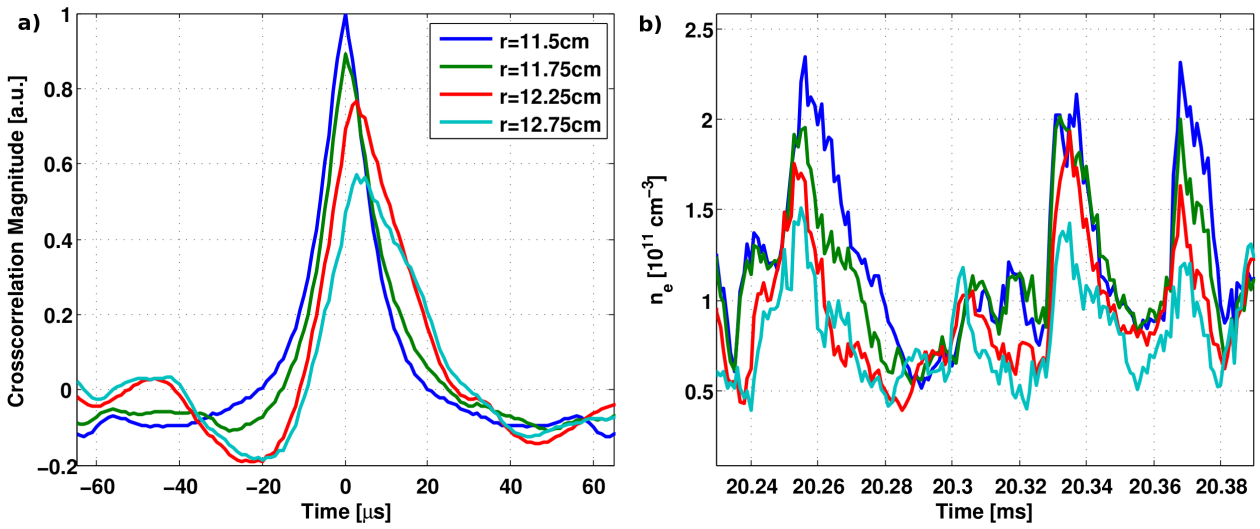

Figure 5.6: Cross-correlation of plasma density fluctuations (a) and close-up density signal (b) showing typical asymmetric spikes. The legend in (a) applies also to (b).

Similarly to the floating potential fluctuations there is a slow decay in spectral density between 30-40 kHz and a sharp edge at 100 kHz. Fitting the mean of all six spectra to a power law with $P \approx f^{-6.4}$. Other toroidal magnetic fusion devices found similar power spectra, however the transition frequency and the exponent in the power law depend on the machine size and underlying dynamics of the plasma turbulence in each machine [35, 36]. In STOR-M, the density turbulence decreases much faster ($f^{-6.4}$) than floating potential fluctuations ($f^{-3.18}$).

The probability density function (PDF) is a histogram, normalized by the length of the time window. Each value of the I_{sat} is assigned to one of the 100 bins, which are equally spaced from the minimum to the maximum value of the I_{sat}. The number of counts per bin over the total number of points gives the probability of the I_{sat} being at this level. In the following part, three basic shapes of PDFs are presented and analysed. Since the shape of a PDF can be represented by the skewness of the PDF, skewness profiles of the density are presented subsequently.

The PDFs of a 2 ms window for different locations are shown in Figures 5.8 (a)-(c), with a Gaussian PDF as reference. For the (a) and (c) only the positive and negative half of the data points were used for the Gaussian fit, respectively. In this way the deviations from the Gaussian PDF with a zero skewness are more visible. The time frame was chosen at the beginning of the flat top of similar discharges. Figure 5.8 (a) shows an asymmetric PDF with a deviation from the Gaussian curve on the negative side. This results in a negative skewness of $S = -0.23$ at a radial position of

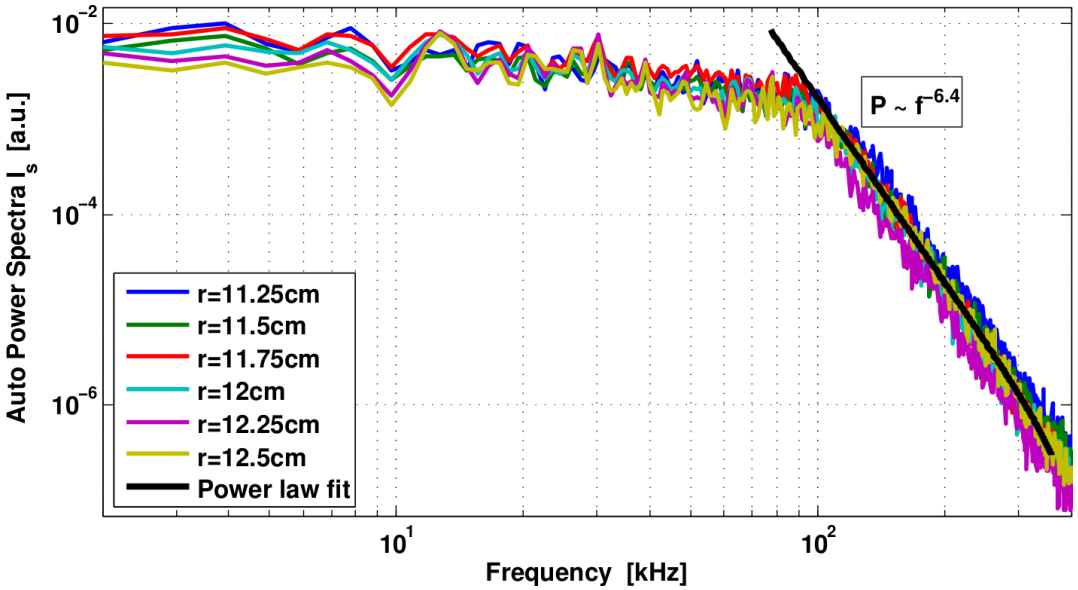

Figure 5.7: Autopower spectrum of six ion saturation current fluctuation signals with power law fit for the averaged signal after 200 kHz, shot 247614.

$r = 9.5$ cm. which means that more negative than positive events are observed in the signal. Figure 5.8 (b) shows a PDF, which is almost symmetric with a skewness of $S = -0.02$. At the plasma edge/SOL transition the PDF shows a positive skewness of $S = 1$ as can be seen in Figure 5.8 (c). The negative tail of the PDF is showing events up to 2.5σ, while in the deep edge at $r = 9.5$ cm almost -4σ were reached. Even more drastic is the change on the positive tail, increasing from $< 3\sigma$ to a large positive tail ending at 5σ. Since positive events are defined by increased plasma densities and negative events by lower densities, positive and negative spikes are referred to as blobs and holes, respectively. Thus regions with positive and negative skewness are accumulations of blobs and holes, respectively. The transition region with equal amounts of blobs and holes, thus having a skewness of zero, is the origin of blob/hole pairs. While the positive skewness is present in most measurements, negative skewness is restricted to deeper edge positions and thus not easy accessible. Figures 5.8 (d)-(f) show the first 800 μs of the raw signals, which were used for the PDFs. Since the difference in skewness for the PDF in Figures 5.8 (a) and (b) is only 0.2, the raw data differs only slightly, however there are more frequent negative spikes visible in Figure 5.8 (a). In Figure 5.8 (b) the repetition rate of the spikes is lower than in Figure 5.8 (a), but blobs and holes are observable in equal measure. The average density in Figure 5.8 (c) is increased by large blobs, thus density levels below the average are not necessarily holes, but rather represents the background

density.

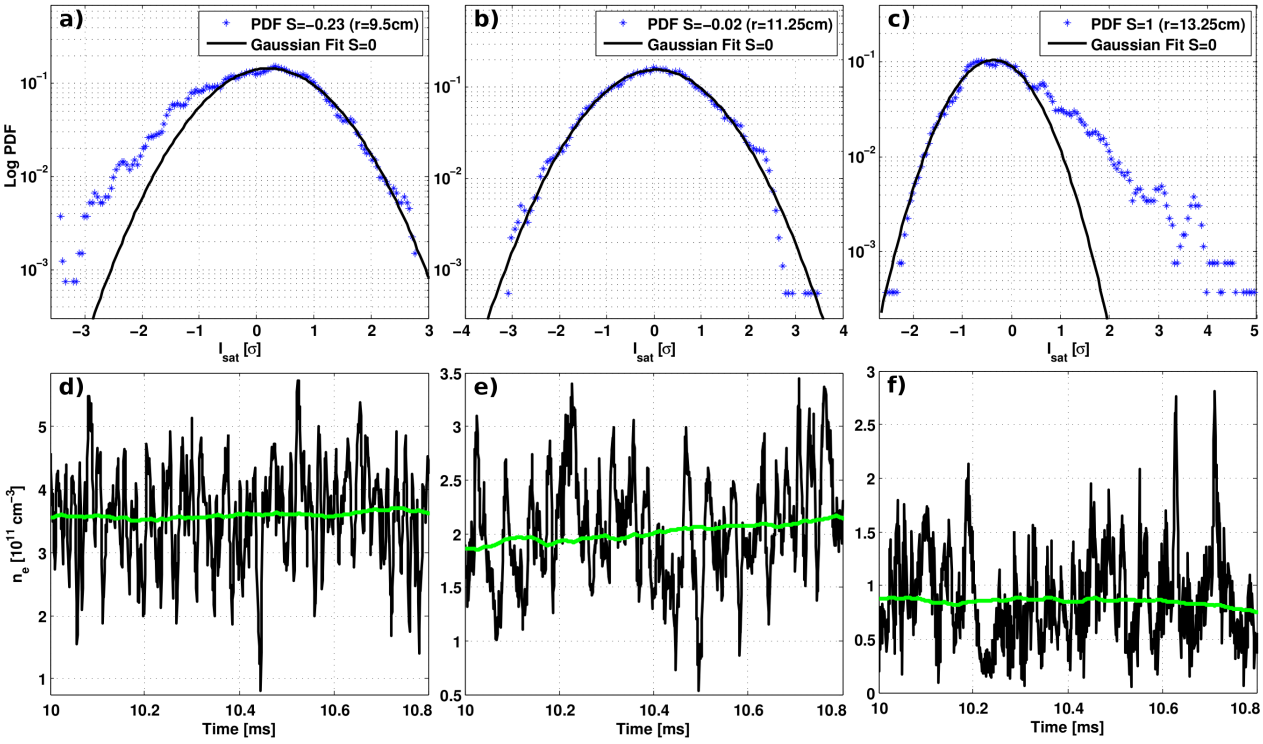

Figure 5.8: PDFs of a 2 ms time frame at different radial positions with Gaussian fits as comparison in (a)-(b). Deviations from the Gaussian curve on the left (negative) in (a) indicate holes, while on the right (positive) in (c), the deviations indicate blobs. The corresponding raw signals of the first 800 μs are shown in (d)-(f) with a 500 μs running average in green.

A set of similar discharges (252979-253004) was used to construct profiles of the plasma density and the skewness of the plasma density fluctuations. Figures 5.9 (a) and (b) show these profiles for 2 ms windows starting at 10 ms and 15 ms from $r = 9.5$-15.25 cm. Both plasma density profiles show a monotonically increasing density, however the profile at $t = 10$-12 ms is steeper inside $r \leq 12$ cm. This change in steepness is caused by a decrease of the overall plasma density over time during the discharge. The plasma density in the SOL region is slightly different, but still within the errorbars. The skewness profiles of the plasma density fluctuations in Figures 5.9 (b) show drastic differences. The skewness profile of the earlier time window is flat in the region outside $r \geq 12$ cm at a skewness of $S \approx 0.8$ and decreases inside the deep edge region to a $S = -0.1$ at $r = 9.5$ cm. The later time window at $t = 15$-17 ms shows the opposite behaviour with an increase of the skewness towards the deep edge region, reaching a skewness of $S \approx 1.2$.

The analysis of the PDFs demonstrated that a negative skewness is an indication for hole accu-

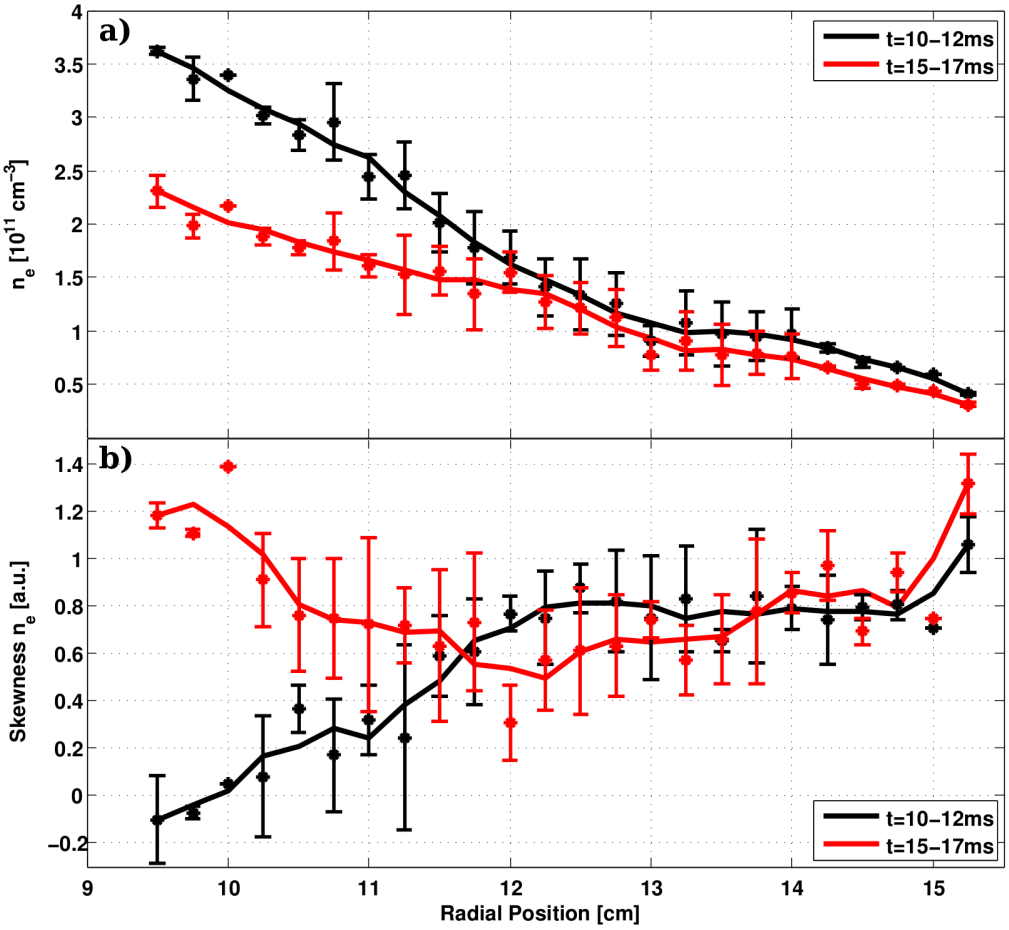

Figure 5.9: Profiles for the plasma density (a) and the skewness of the plasma density (b) at two different time windows during the current flat-top phase.

mulation, thus the deep edge region during $t = 10$-12 ms is the beginning of a hole accumulation zone. The extent of this zone is unclear, since the rake probe could affect the discharge or could be damaged at positions deeper inside the plasma. The birth region of blob/hole pairs is located at the zero transition of the skewness,thus at $r \approx 10$ cm in this case. For the second time frame no decrease of the skewness is visible in the deep edge, therefore it is assumed that the blob/hole birth zone is located much deeper inside the plasma. In other tokamaks, the hole accumulation zone was located just at the inside of the last closed flux surface and well out of the region accessible for Langmuir or rake probes [37, 38, 39]. Whether the hole accumulation zone is accessible by internal probes in STOR-M seems to depend on the overall plasma density in the tokamak, while the plasma position could be an important factor as well.

5.3 Geodesic Acoustic Mode

The high frequency branch of the zonal flow phenomenon is called GAM and is found commonly in the edge region of tokamaks. The specific frequency connected to GAM is $f_{\mathrm{GAM}} \approx \frac{\sqrt{2}}{2\pi}\frac{C_s}{R} \approx 20$ kHz for typical STOR-M edge parameters. The majority of discharges shows a broadband auto-power spectrum of the floating potential with multiple peaks, but no consistency in frequency. Therefore the absence of GAM in STOR-M was assumed. However rare discharges show features in the auto-power spectrum, which need to be examined in more detail.

Figure 5.10 shows the auto-power spectra of the floating potential fluctuations for shot 252072 at six different radial locations and one additional auto-power spectrum for a Mirnov coil signal. The time window for the auto-power calculation was $t = 10$-25 ms. The spectrum shows no distinct peak, but a higher fluctuation amplitude in the frequency range of $f \approx 15$-23 kHz for the innermost rake probe pins. With increasing radial position the elevated fluctuation amplitude becomes less pronounced and fades into the background fluctuations. The Mirnov coil signal has a broad peak at about 35-40 kHz and shows only small fluctuation amplitudes, where the maximum amplitudes of the floating potential fluctuations are. It is shown as a comparison, because MHD oscillations have global oscillation modes in the obvious 35-40 kHz range, but also at lower frequencies [40], which correspond to the broad peak in the floating potential spectrum. In order to distinguish whether the increased fluctuation amplitude in the floating potential spectrum is caused by MHD oscillations or

by the GAM, will be addressed by the following analysis.

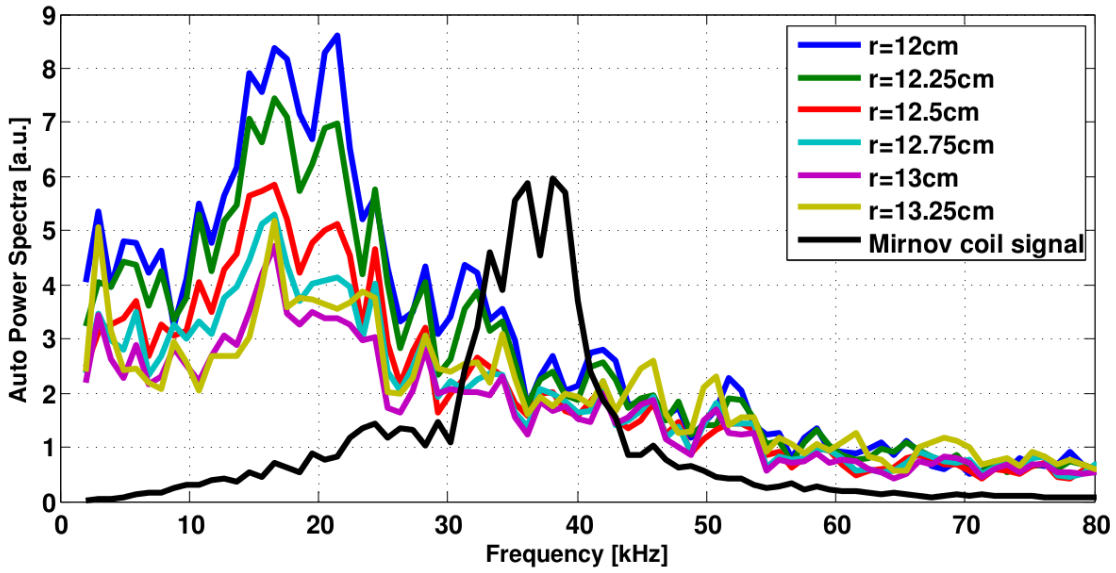

Figure 5.10: Auto-power spectra of a Mirnov coil signal and floating potential fluctuations at the indicated locations.

Figure 5.11 shows the fluctuation amplitude over time and frequency based on a wavelet auto-power calculation. Since the time window is the same as for the auto-power spectra in Figure 5.10, it is seen that the broad maximum in the fluctuation amplitude spectrum stems from individual, short peaks at different frequencies. While the intermittent character of GAMs was found in other tokamaks [16], the frequency remained constant. Here, the frequency jumps to different values, which would correspond to fast changing temperatures, since the GAM frequency is temperature dependent.

Figure 5.12 (a) shows the frequency resolved coherence of the floating potential fluctuations over the distance to the innermost rake probe pin. During the flat-top phase of the discharge, eight subwindows of 1 ms length were used to evaluate the coherence at $t = 16$-18 ms. The subwindows were equally spaced and multiplied with a hamming window to lower the influence of the overlapping parts. A broad region around $f = 20$ kHz shows increased coherence and is still above 0.7 after a distance of $\Delta r = 1.25$ cm, while other narrow bands with increased coherence exist. Besides those narrow band the coherence drops quickly at higher frequencies after 0.5 cm. This observation demonstrates, that high frequency turbulence eddies extend in a very short radial distance of less than 0.5 cm. The low frequency oscillations at ≈ 20 kHz extend to a larger radial distance ≥ 1.25

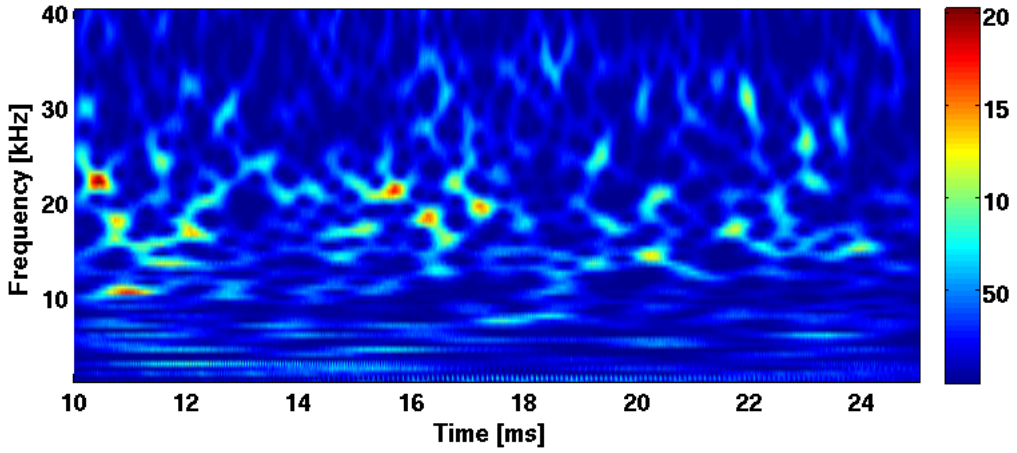

Figure 5.11: Wavelet auto-power amplitude of the floating potential fluctuation at $r = 12$ cm in discharge 252072. The colour bar represents the fluctuation amplitude.

cm.

In Figure 5.12 (b) the reference signal for the coherence calculation is the Mirnov coil signal. At $f = 20$ kHz the MHD oscillation is clearly coherent to all rake probe pins. This strongly suggests, that MHD oscillations are visible in the floating potential spectrum, since GAM is electrostatic and therefore not observable by Mirnov coils. On the other hand, there is no coherence between the Mirnov signal and the floating potential in the frequency range of the high amplitude MHD oscillation around 35-40 kHz. Thus the causal connection between the observed coherence is not clear at this moment. Interestingly, the coherence increases slightly from the innermost to the outermost pin, although the amplitude at this frequency in the floating potential fluctuation spectrum decreases with increasing radial position.

Other features of GAM that could test the existence of GAM include the poloidal and toroidal mode symmetry of the oscillation, which corresponds to the poloidal and toroidal mode number of $(m = 0)$ and $(n = 0)$, respectively. Radially, GAMs are localized and thus a deeper edge measurement would see an increase and subsequent decrease in fluctuation amplitude, but this has not been observed.

5.4 Effect of RMP

The RMP field is applied to suppress MHD fluctuations of a certain mode structure, which is determined by the path of the coils around the vacuum vessel. If the coils match the helicity of

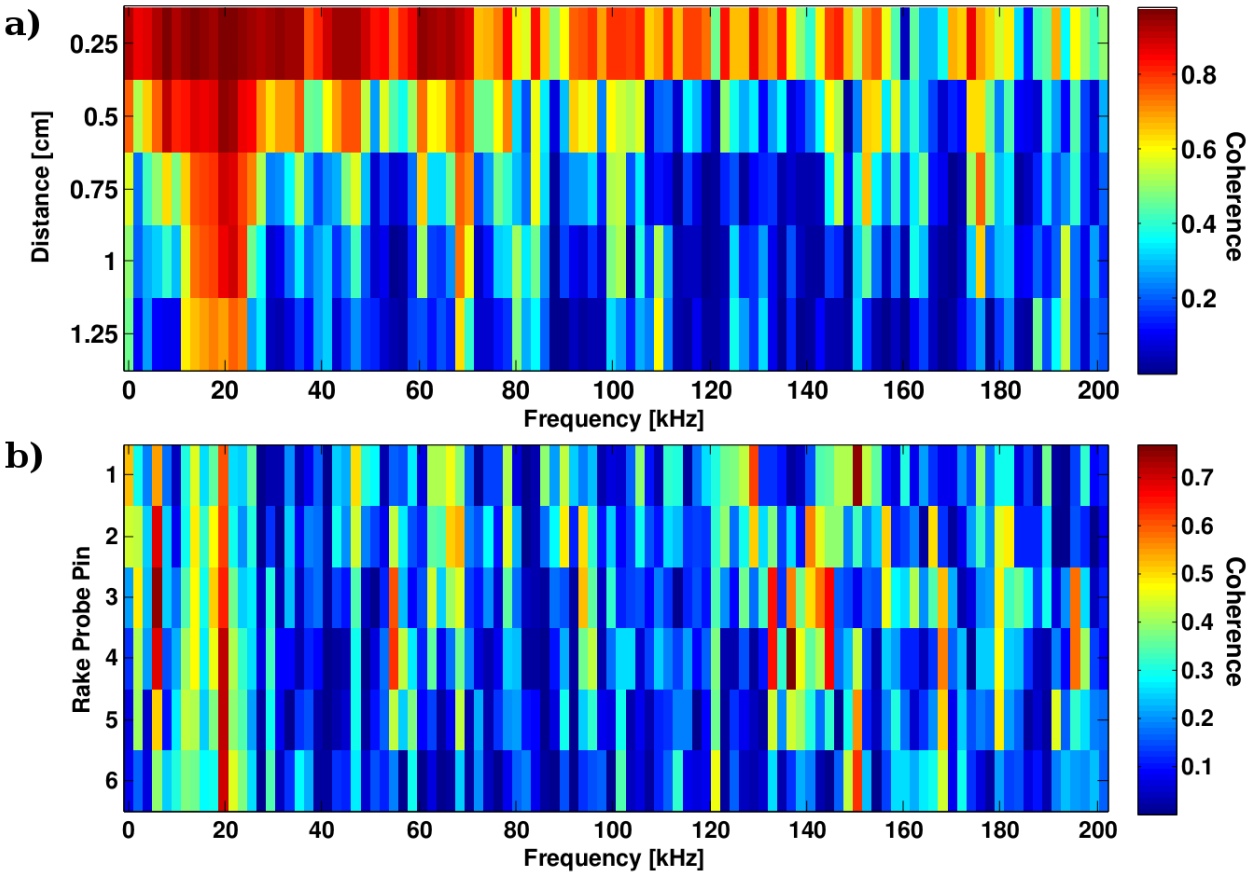

Figure 5.12: Frequency resolved coherence over distance with reference in (a) to the innermost rake probe pin at $r = 12$ cm and for (b), the Mirnov coil signal is used as the reference.

the rotating islands in the magnetic field, the islands are slowed down and suppressed for the time of the RMP. During this experiment either one pulse of 8 ms or two 3 ms pulses with a 2 ms break in between were used to study the effect of the RMP on the plasma parameters. The present configuration affects the $(m = 2)$,$(n = 1)$-mode of MHD fluctuations [27]. An example for MHD suppression is shown in Figure 5.13, where the waveforms of the RMP current (a) and the Mirnov coil signals $\dot{\tilde{B}}_\theta$ are shown without RMP in Figure 5.13 (b) and without RMP (c). The wavelet analysed auto-power spectrum of the Mirnov signals are shown on the right side in Figure 5.13 (d) and (e). With about 1-1.5 ms delay from the start of the RMP pulse, the amplitude of the raw Mirnov coil signals decreases clearly and the wavelet auto-power shows a strong decrease to the background level between $f \approx$ 30-40 kHz. During the discharge the $(m = 2)$-mode was dominant, thus the suppression is observable. In the following part of this Section, the effect of the RMP on floating potential, plasma density and deduced/derived quantities is investigated. The current level of the applied RMP pulse is always given as the average value during the main part of the pulse. However, a premature decline as in Figure 5.13 (a) after $\approx$ 26 ms is not included in the average, since it would be misleading for evaluating the strength of the RMP pulse.

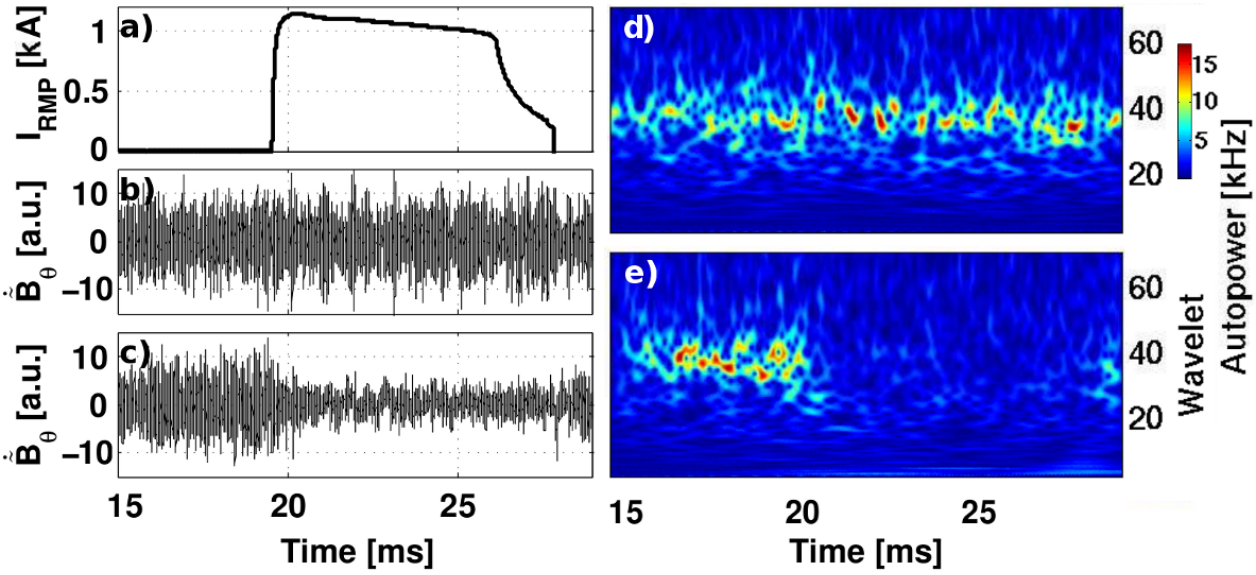

Figure 5.13: Waveforms of RMP current (a), raw Mirnov coil signals and wavelet auto-power of Mirnov coil signals for the case without RMP (b, d) and with RMP (c, e).

5.4.1 Floating Potential

Figure 5.14 shows the main parameters of similar discharges, with the last trace being the current in the RMP coils. None of the parameters show a noticeable change, except for the plasma position, where the grey area indicates the time in which the RMP is switched on. The lower trace of the plasma position corresponds to the discharge without RMP, while the position increases towards positive ΔH with increasing RMP current. The outwards shift of the plasma takes about 1.5 ms to reach its maximum and is delayed to the maximum of the RMP current by about 1 ms. Comparing the discharge with and without RMP, the maximum change in position is 4 mm.

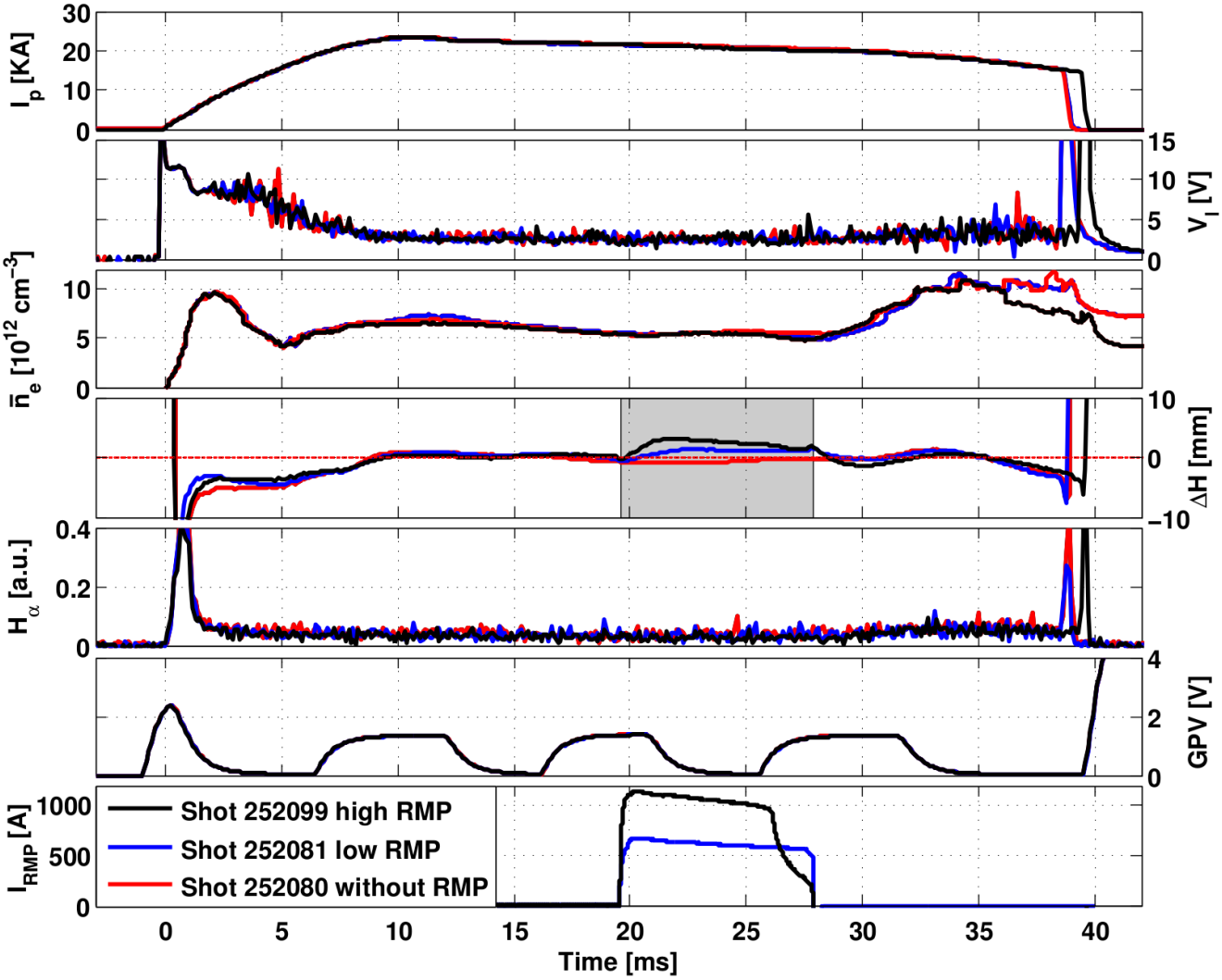

Figure 5.14: Main discharge parameters for three different shots without RMP in red, low RMP current in blue and high RMP current in black.

Figure 5.15 shows the profile of the floating potential without and with RMP at different current levels. The profiles were constructed from a number of similar discharges with reproducible plasma conditions. Six pins of the rake probe were monitoring the floating potential at different radial positions, and for constructing the profiles all of the signals were averaged according to their position. Without RMP the floating potential is monotonically increasing from the far SOL to the edge region as can be seen from the dark blue curve. Increasing the RMP current to 620 A shows no effect in the region of measurements, but a further increase to 880 A causes a slight flattening of the profile around the limiter at $r = 12$-13 cm. A clear change can be seen at the highest current level at 1040 A, where a broad region from $r = 12.5$-14 cm shows a flat floating potential profile and starting from $r \approx 12.5$ cm a steep floating potential drop is visible.

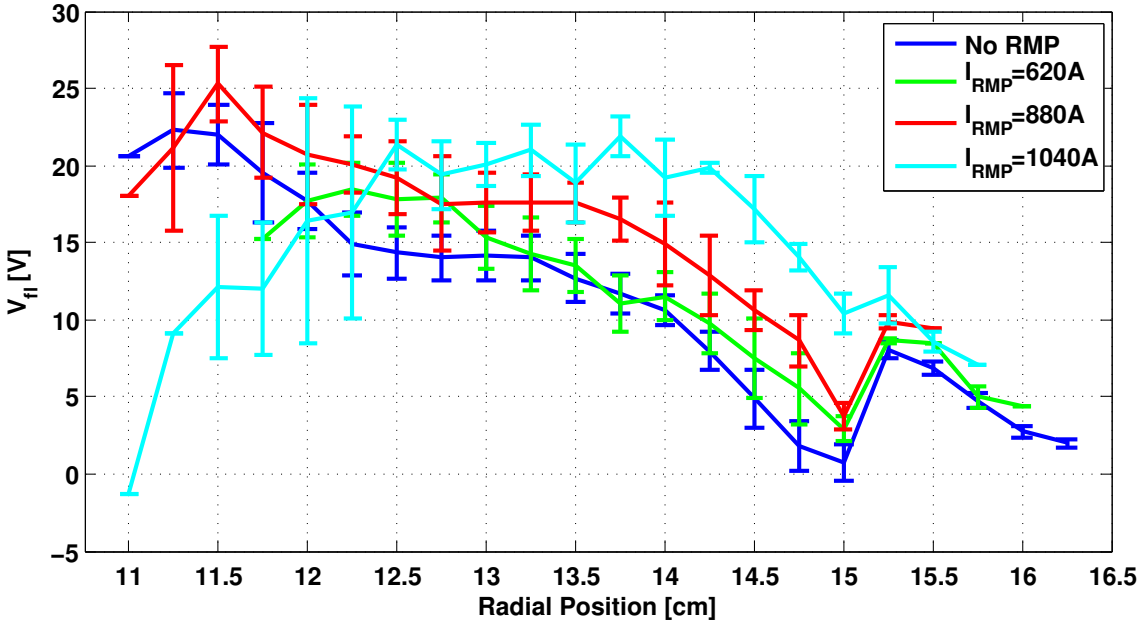

Figure 5.15: Profile of the floating potential for different RMP currents.

A very similar influence can be seen in the amplitude of the floating potential fluctuations in Figure 5.16. In the SOL region the RMS of the floating potential fluctuations is increasing with the RMP current level, while in the edge region the effect is reversed. At the highest two RMP levels, the RMS value peaks and declines slightly towards the center direction. At 1040 A, the RMP seems to steepen the potential profile and reduce turbulence in the edge region, which is usually accompanied by improved confinement.

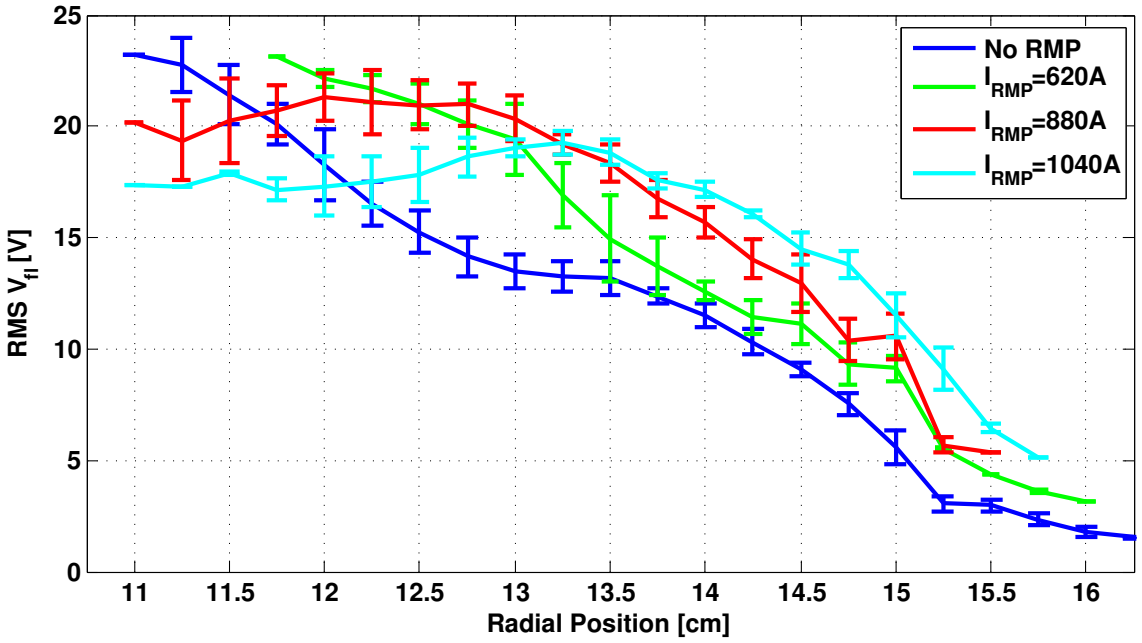

Figure 5.16: Profile of the RMS floating potential fluctuations for different RMP currents.

5.4.2 Ion Saturation Current

The main parameters and the density waveforms of two similar discharges are shown in Figure 5.17, where the RMP pulse was applied only during one of the discharges. The RMP waveform on the highest setting is shown in the last row, where the current in the RMP coils exceed 1000 A. The density waveforms at $r = 12$ cm and $r = 12.75$ cm show an increase during the whole application of the RMP pulse, while the line averaged density is unaffected.

Figure 5.18 shows profiles of the density for different RMP currents. The discharge conditions are similar to the previous examples, except the RMP pulse was applied at a later time from $t =$ 19.5-28 ms. The line averaged density and edge/SOL density are reduced by $\approx 20\%$ compared to the discharges presented in the previous Sections, due to different gas puff settings and the later time frame at $t = 22$-26 ms. The profile was constructed by a series of discharges, taking the mean value of the 4 ms windows at the same rake probe pin positions. Applying the RMP field causes a density increase from the edge region throughout the whole SOL region. After $r = 14.5$ cm the density gradient becomes steeper as the pedestal density level increases with the RMP current, but no steepening of the profile is visible in the edge and SOL region.

An overview of how the mean density in the edge/SOL region increases with RMP current can

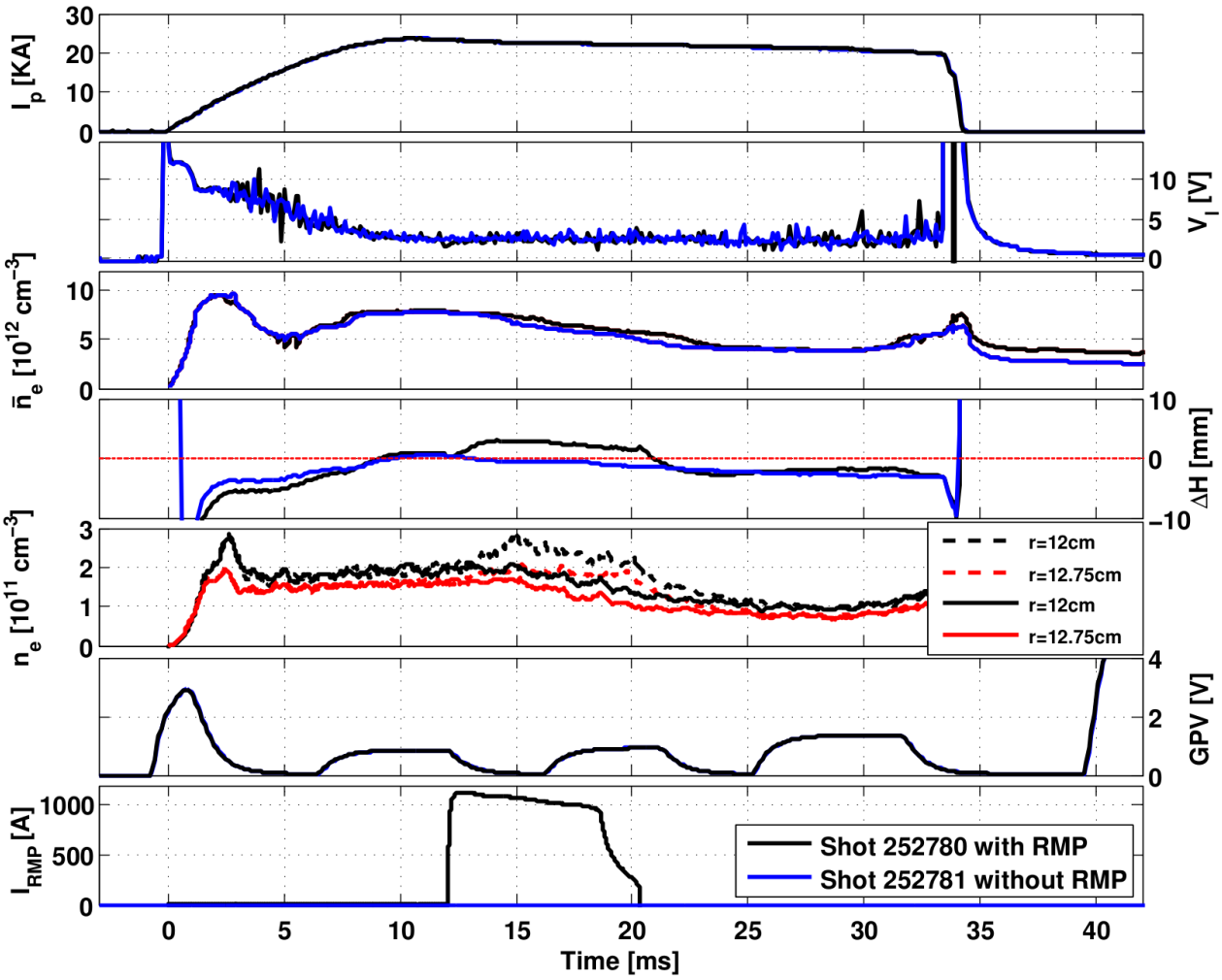

Figure 5.17: Discharge parameters for two different discharges with RMP in black and without RMP in blue. The waveforms of the edge density are shown for two radial positions with dashed lines indicating the discharge with RMP and solid lines without RMP.

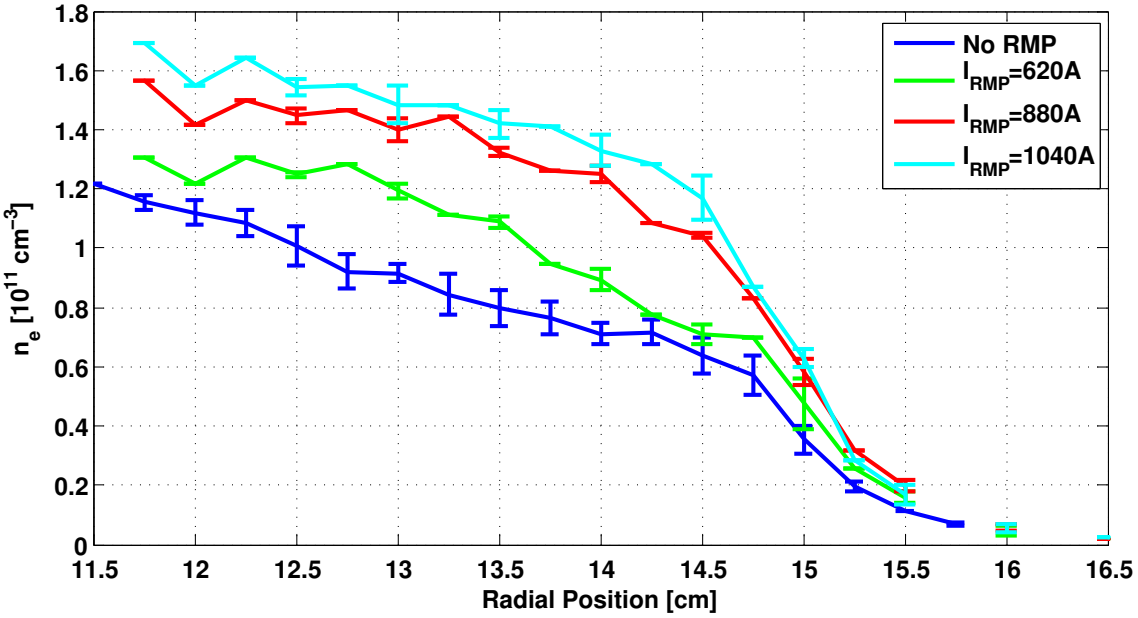

Figure 5.18: Profile of the density for different RMP currents at $t = 22$-26 ms.

be seen in Figure 5.19. The upper and lower curves originate from discharges 252063-252104 and 252712-252780 with one long (≈ 8 ms) RMP pulse, while the middle two are measured during the first and second pulse of discharges 252814-252836 with two 3 ms pulses. Starting from different initial densities, the increase with RMP current is nearly linear and does not show a saturation at high currents. Maximum RMP currents of $I_{\mathrm{RMP}} \approx 1$ kA were limited by the switching system and the capacitors.

To clarify the reason behind the density increase, further analysis of the data is performed to characterize the edge and SOL region. In Figure 5.20 the response of the density fluctuation skewness is shown by profiles at different RMP currents. As mentioned before, the skewness of the density fluctuations is a measure of how many high amplitude events are happening with respect to the background level. A positive value indicates a dominance of positive spikes, also called blobs. A Gaussian, i.e. symmetric distribution has a skewness of zero and thus blobs and holes are occurring at similar rates. Without the application of a RMP pulse the skewness is rather flat, with a slight increase in the edge region and larger values after $r = 14.5$ cm, where the density declines significantly. As the background density becomes lower, the blobs have a larger effect on the skewness calculation. The RMP affects the edge and SOL region visibly: the skewness drops at the lowest RMP setting, reaching $S = 0.1$ and increases with increasing RMP current to the original

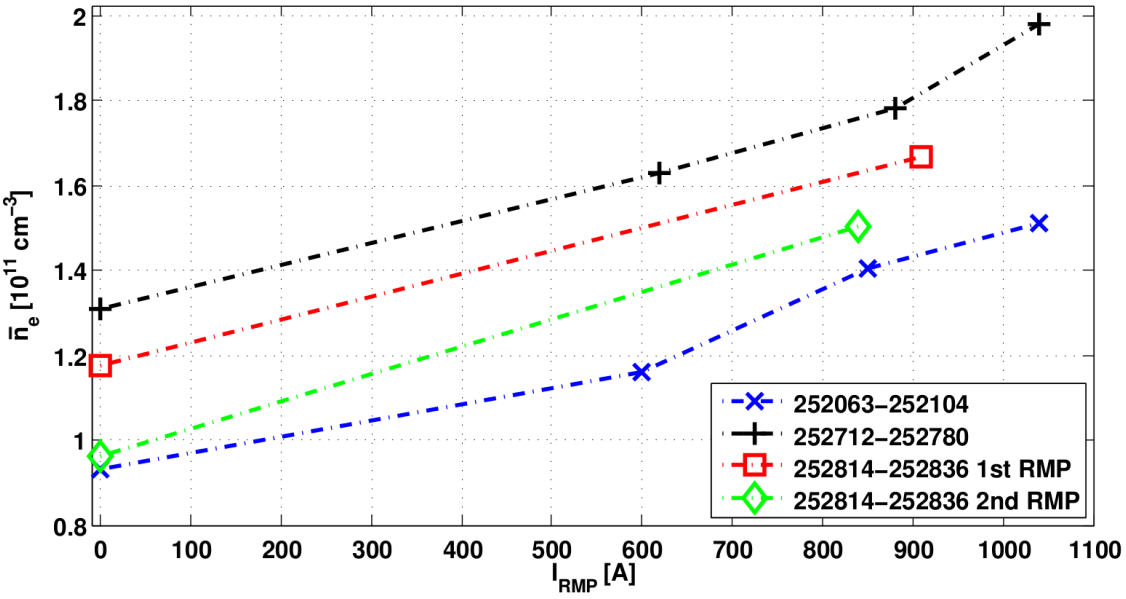

Figure 5.19: Mean density in the SOL/edge region plotted against RMP current for different discharge conditions and RMP waveforms. The indicated range of discharges was used to obtain the average density values from the density profiles.

level of about $S = 0.5$. However, the skewness in the edge region increases and reaches a plateau of $S = 1.0 - 1.2$. The transition region, where the skewness increases, moves radially outside with increasing RMP current.

Another measure for the plasma transport is the turbulent flux $\Gamma = \tilde{n}\tilde{E}_\theta/B$, with $\tilde{n}$ and $\tilde{E}_\theta$ being the fluctuating part of the plasma density and poloidal electric field, respectively. Since there are two rows of pins, poloidally separated by 2.5 mm, using both pins of a certain radial position to measure the floating potential fluctuations is utilized to calculate the poloidal electric field fluctuations. This in turn leads to the fluctuating part of the radial velocity via $\tilde{v}_r = \tilde{E}_\theta/B$.

Consequently, the probe tips at the third and fifth radial position were both used as floating potential pins. In addition to the density measurements at the second, fourth and sixth position, for a total of four points the turbulent flux is estimated. Looking at a particular time window, there will be positive and negative events, depending on the phase difference between density and electric field fluctuations. For constructing the profile, the mean value is calculated, thus averaging over inwards and outwards fluxes.

Figure 5.21 shows the turbulent flux profile for similar discharges with different RMP currents applied. The RMP pulse clearly enhances the turbulent flux, but interestingly the increase is greater

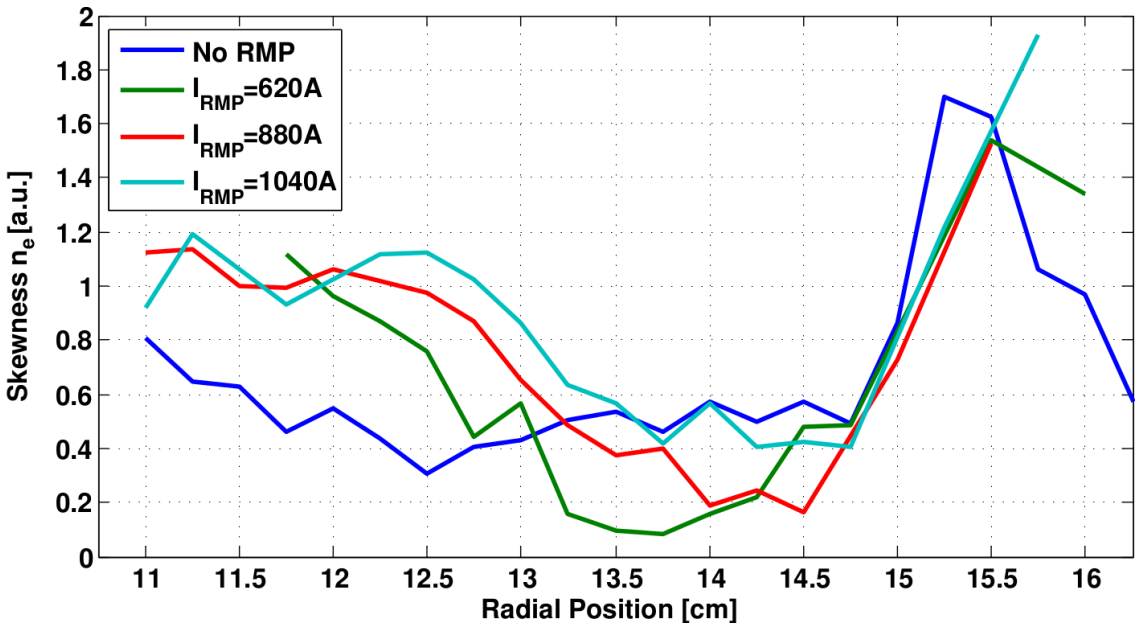

Figure 5.20: Skewness density fluctuation profile for different RMP currents at t = 14-18 ms.

in the edge region around $r \approx 12$ cm and in the far SOL $r \approx 14.5$ cm. No threshold seems to exist, since the increase of the turbulent flux is visible at the lowest RMP current level.

The increase of the skewness and the turbulent flux suggests, that the increased density is caused by an increase of cross-field particle transport. Especially the intermittent transport consisting of blobs is contributing, which can be desirable in a fusion reactor, since it helps to remove the "ash" of the fusion reaction.

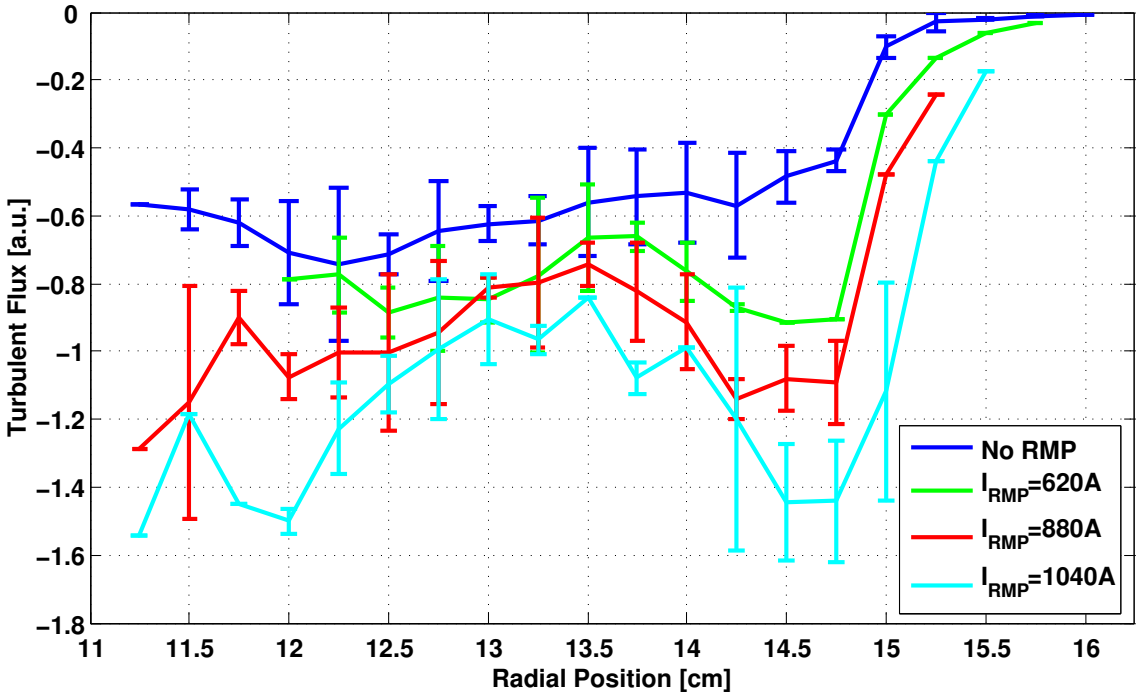

Figure 5.21: Turbulent Flux profile for different RMP currents at $t = 14$-18 ms.

CHAPTER 6

CONCLUSION AND SUMMARY

In order to analyse the spatio-temporal properties of plasma density and potential fluctuations a movable 16 pin rake probe was installed at STOR-M to construct profiles of ion saturation current and floating potential. Additional signal processing methods gave access to various plasma parameters and fluctuation properties of the measured quantities. The effect of an RMP pulse on the edge plasma was analysed and compared to normal Ohmic discharges without RMP. Different discharge conditions were examined to find evidence for the GAM oscillations in the floating potential fluctuation signal and distinguish it from MHD oscillations. Measurements were taken at deep edge locations down to $r = 9.5$ cm to get additional insight about the origin of blobs/holes. Profiles of plasma density fluctuation skewness show, for most discharge conditions in the plasma edge and all conditions in the SOL region, positive values in the range of $S = 0.5 - 1$, indicating a dominance of intermittent transport events called blobs. For one experimental set up, the increased overall plasma density led to the observation of a negative skewness down to $S = -0.2$ at the deepest measurement position at $r = 9.5$ cm. Hence, this is the start of the hole accumulation region and the zero crossing of the skewness is the birth region of blob/hole pairs. During normal ohmic discharges, this region is too deep for rake probe measurements.

The effect of the RMP on the density is independent of its pulse length and does not depend on whether a single long pulse or two short double pulses are applied. The density in a wide range from edge to SOL is increasing proportionally to the current in the RMP coils, showing no saturation up to a current level of $I_{\mathrm{RMP}} = 1040$ kA. Since the line averaged density is not changing due to the RMP pulse, the density profile is assumed to be flattening out and thus increasing the density pedestal in the edge and SOL. While the increase of the turbulent flux suggests that a higher particle transport is responsible for the density increase, features like fluctuation suppression and shortening of the lifetime of coherent structures at deeper edge locations were observable.

The response of the floating potential depends on the experimental set up. A potential drop and appearance of a negative electric field was visible for some discharge conditions. The fluctuation amplitude of the floating potential was generally increased in the SOL and edge region close to the limiter and decreased further inside the plasma.

An oscillation at the GAM frequency, corresponding to STOR-M edge parameters could be observed. The coherent structure has a radial extent of ≥ 1 cm, but it is also coherent to the low frequency part of MHD oscillations.

6.1 Future Work

The rake probe is currently installed on STOR-M and in working condition. Further experiments with the RMP are planned and can further analyze the response of the edge and SOL plasma. A higher current for the RMP could test if there is a saturation of the effects on density and floating potential. Temperature measurements should verify the assumption of negligible temperature fluctuations and test the effect of the RMP field on the equilibrium temperature in the edge.

The rake probe pin configuration used during the experiments permit additional analysis, for example the Reynolds stress can be estimated for every set of three pins, that allows simultaneous measurements of the electric field fluctuations in poloidal and radial direction, thus giving access to radial and poloidal velocity fluctuations. The Reynolds stress tensor $R_{\theta,r} = \langle \tilde{v}_\theta \tilde{v}_r \rangle$ measures the correlation between poloidal and radial fluctuations, which plays a role in poloidal flow generation when the Reynolds stress shows a radial gradient.

The investigation of GAM is inconclusive so far. If a distinct oscillation mode exists in STOR-M, it can be shown by better methods of data analysis and discharge conditions suitable for GAM generation. Tokamaks of similar size verify GAM indirectly by long range correlations and via a phase relation between distant floating potential measurements. Further employment of invasive and non-invasive probes is needed to identify GAM unambiguously.

REFERENCES

[1] Data: United Nations, "World Population Prospect: The 2010 Revision." www.weltbevoelkerung.de/uploads/tx_tspagefileshortcut/WBprojektionen_bis_2100_nach_WPP_2010_Kurven.pdf, Oct 2012. Adopted from DSW graphic.

[2] T. Hamacher, "Annual global electricity production with a CO2 restriction of 550 ppm." www.ipp.mpg.de/ippcms/de/for/projekte/energie/index.html, Oct 2012.

[3] F. Wagner, G. Becker, K. Behringer, D. Campbell, *et al.*, "Regime of Improved Confinement and High Beta in Neutral-Beam-Heated Divertor Discharges of the ASDEX Tokamak," *Physical Review Letters*, vol. 49, pp. 1408–1412, Nov 1982.

[4] J. Linke, T. Loewenhoff, V. Massaut, G. Pintsuk, *et al.*, "Performance of different tungsten grades under transient thermal loads," *Nuclear Fusion*, vol. 51, Jul 2011.

[5] S. Atzeni and J. Meyer-ter Vehn, *The Physics of Inertial Fusion*. Oxford University Press, USA, 2004.

[6] S. Nakai and H. Takabe, "Principles of inertial confinement fusion - Physics of implosion and the concept of inertial fusion energy," *Reports on Progress in Physics*, vol. 59, pp. 1071–1131, Sep 1996.

[7] R. C. Wolf and W.-X. Team, "Wendelstein 7-X: An Alternative Route to a Fusion Reactor," *Contributions to Plasma Physics*, vol. 49, no. 9, pp. 671–680, 2009.

[8] K. Hirl, "Nuclear fusion - status and perspectives." online Booklet, www.ipp.mpg.de/ippcms/eng/pr/publikationen/broschueren/, 2011.

[9] J. Wesson, *Tokamaks*. The International Series of Monographs on Physics, Oxford University Press, USA, 2004.

[10] F. F. Chen, *Introduction to Plasma Physics and Controlled Fusion*. Plenum Press, 2nd ed., 1984.

[11] www.dpg-physik.de/dpg/gliederung/fv/p/info/pix/Tokamak.jpg, Oct 2012.

[12] W. Horton, "Drift waves and transport," *Reviews of Modern Physics*, vol. 71, pp. 735–778, Apr 1999.

[13] T. Windisch, *Intermittent Events and Structure Propagation in Plasma Turbulence*. PhD thesis, Ernst-Moritz-Arndt-University Greifswald, 2007.

[14] N. Winsor, J. L. Johnson, and J. M. Dawson, "Geodesic Acoustic Waves in Hydromagnetic Systems," *Physics of Fluids*, vol. 11, no. 11, pp. 2448–2450, 1968.

[15] P. H. Diamond, S.-I. Itoh, K. Itoh, and T. S. Hahm, "Zonal flows in plasma - a review," *Plasma Physics and Controlled Fusion*, vol. 47, no. 5, p. R35, 2005.

[16] A. Fujisawa, "A review of zonal flow experiments," *Nuclear Fusion*, vol. 49, no. 1, p. 013001, 2009.

[17] G. D. Conway, C. Tröster, B. Scott, and K. H. et al., "Frequency scaling and localization of geodesic acoustic modes in ASDEX Upgrade," *Plasma Physics and Controlled Fusion*, vol. 50, no. 5, p. 055009, 2008.

[18] L. G. Askinazi, M. I. Vildjunas, N. A. Zhubr, A. D. Komarov, *et al.*, "Evolution of geodesic acoustic mode in ohmic H-mode in TUMAN-3M tokamak," *Technical Physics Letters*, vol. 38, pp. 268–271, Mar 2012.

[19] C. Silva, P. Duarte, H. Fernandes, H. Figueiredo, and I. N. et al., "Characterization of geodesic acoustic modes in the ISTTOK edge plasma," *Plasma Physics and Controlled Fusion*, vol. 51, no. 8, p. 085009, 2009.

[20] T. S. Hahm, "Physics behind transport barrier theory and simulations," *Plasma Physics and Controlled Fusion*, vol. 44, no. 5A, p. A87, 2002.

[21] A. I. Smolyakov, P. H. Diamond, and V. I. Shevchenko, "Zonal flow generation by parametric instability in magnetized plasmas and geostrophic fluids," *Physics of Plasmas*, vol. 7, no. 5, pp. 1349–1351, 2000.

[22] Y. Hamada, T. Watari, A. Nishizawa, O. Yamagishi, and K. N. et al., "GAM generation by drift waves in JIPP T-llU tokamak core plasmas," *Nuclear Fusion*, vol. 50, no. 2, p. 025001, 2010.

[23] A. Hirose, C. Xiao, O. Mitarai, J. Morelli, and H. Skarsgard, "STOR-M tokamak design and instrumentation (invited)," *Physics in Canada*, vol. 62, pp. 111–120, 2006.

[24] W. Zhang, C. Xiao, G. D. Conway, O. Mitarai, *et al.*, "Improved confinement and edge plasma fluctuations in the STOR-M tokamak," *Physics of Fluids B: Plasma Physics*, vol. 4, no. 10, pp. 3277–3284, 1992.

[25] C. Xiao and A. Hirose, "The Role of Plasma Biasing in the H-Modes in the STOR-M Tokamak," *Contributions to Plasma Physics*, vol. 40, no. 1-2, pp. 184–189, 2000.

[26] C. Xiao, A. Hirose, and S. Sen, "Improved confinement induced by tangential injection of compact torus into the Saskatchewan Torus-Modified (STOR-M) tokamak," *Physics of Plasmas*, vol. 11, no. 8, pp. 4041–4049, 2004.

[27] S. Elgriw, D. Liu, T. Asai, A. Hirose, and C. Xiao, "Control of magnetic islands in the STOR-M tokamak using resonant helical fields," *Nuclear Fusion*, vol. 51, Nov 2011.

[28] V. I. Demidov, S. V. Ratynskaia, and K. Rypdal, "Electric probes for plasmas: The link between theory and instrument," *Review of Scientific Instruments*, vol. 73, no. 10, pp. 3409–3439, 2002.

[29] F. F. Chen, "Electric probes," in *Plasma Diagnostic Techniques* (H. Huddelstone, ed.), New York: Academic, 1965.

[30] G. M. R. St. Germaine, "Plasma flow velocity measurements with a Gundestrup Probe in the STOR-M Tokamak," Master's thesis, University of Saskatchewan, Jul 2006.

[31] J. E. Morelli, *Plasma Position Control in the STOR-M Tokamak: A Fuzzy Logic Approach*. PhD thesis, University of Saskatchewan, Jan 2003.

[32] D. Liu, *Vertical Compact Torus Injection into the STOR-M Tokamak*. PhD thesis, University of Saskatchewan, Nov 2006.

[33] C. Shannon, "Communication in the Presence of Noise," *Proceedings of the IRE*, vol. 37, pp. 10 – 21, jan. 1949.

[34] J. W. Cooley and J. W. Tukey, "An Algorithm for Machine Calculation of Complex Fourier Series," *Mathematics of Computation*, vol. 19, no. 90, pp. 297–&, 1965.

[35] S. J. Zweben, J. A. Boedo, O. Grulke, C. Hidalgo, *et al.*, "Edge turbulence measurements in toroidal fusion devices," *Plasma Physics and Controlled Fusion*, vol. 49, pp. S1–S23, Jul 2007. IEA Large Tokamak Workshop on Edge Transport in Fusion Plasmas, Cracow, POLAND, SEP 11-13, 2006.

[36] M. A. Pedrosa, C. Hidalgo, B. A. Carreras, R. Balbin, *et al.*, "Empirical similarity of frequency spectra of the edge-plasma fluctuations in toroidal magnetic-confinement systems," *Physical Review Letters*, vol. 82, pp. 3621–3624, May 1999.

[37] D. A. D'Ippolito, J. R. Myra, and S. J. Zweben, "Convective transport by intermittent blob-filaments: Comparison of theory and experiment," *Physics of Plasmas*, vol. 18, Jun 2011.

[38] B. Nold, G. D. Conway, T. Happel, H. W. Mueller, *et al.*, "Generation of blobs and holes in the edge of the ASDEX Upgrade tokamak," *Plasma Physics and Controlled Fusion*, vol. 52, Jun 2010.

[39] N. Yan, G. S. Xu, W. Zhang, J. F. Chang, *et al.*, "Observation of Blobs and Holes in the Boundary Plasma of EAST Tokamak," *Plasma Science and Technology*, vol. 13, pp. 410–414, Aug 2011.

[40] S. Gamudi, "Investigation of Magnetohydrodynamic Fluctuation Modes in the STOR-M Tokamak," Master's thesis, University of Saskatchewan, 2009.